Open Research Online

The Open University's repository of research publications
and other research outputs

The AKARI far-infrared all-sky survey maps

Journal Item

oro.open.ac.uk

The AKARI far-infrared all-sky survey maps

Yasuo Doi,[1,*] Satoshi Takita,[2] Takafumi Ootsubo,[1] Ko Arimatsu,[2]
Masahiro Tanaka,[3] Yoshimi Kitamura,[2] Mitsunobu Kawada,[2]
Shuji Matsuura,[2] Takao Nakagawa,[2] Takahiro Morishima,[4]
Makoto Hattori,[4] Shinya Komugi,[2,†] Glenn J. White,[5,6] Norio Ikeda,[2]
Daisuke Kato,[2] Yuji Chinone,[4,‡] Mireya Etxaluze,[5,6]
and Elysandra F. Cypriano[7,5]

[1]Department of Earth Science and Astronomy, The University of Tokyo, 3-8-1 Komaba, Meguro-ku,
Tokyo 153-8902, Japan
[2]Institute of Space and Astronautical Science, Japan Aerospace Exploration Agency, 3-1-1 Yoshinodai,
Chuo-ku, Sagamihara, Kanagawa 252-5210, Japan
[3]Center for Computational Sciences, University of Tsukuba, 1-1-1 Tennodai, Tsukuba, Ibaraki 305-8577,
Japan
[4]Astronomical Institute, Tohoku University, Aramaki, Aoba-ku, Sendai, Miyagi 980-8578, Japan
[5]Department of Physics & Astronomy, The Open University, Milton Keynes, MK7 6BJ, UK
[6]Space Science and Technology Department, The Rutherford Appleton Laboratory, Didcot OX11 0QX, UK
[7]Department of Astronomy, IAG, Universidade de São Paulo, 05508-090 São Paulo, SP, Brazil

*E-mail: doi@ea.c.u-tokyo.ac.jp
[†]Present address: Division of Liberal Arts, Kogakuin University, 2665-1 Nakano-machi, Hachioji, Tokyo 192-0015, Japan.
[‡]Present address: High Energy Accelerator Research Organization (KEK), 1-1 Oho, Tsukuba, Ibaraki 305-0801, Japan.

Abstract

We present a far-infrared all-sky atlas from a sensitive all-sky survey using the Japanese AKARI satellite. The survey covers > 99% of the sky in four photometric bands centred at 65 μm, 90 μm, 140 μm, and 160 μm, with spatial resolutions ranging from 1′ to 1″5. These data provide crucial information on the investigation and characterisation of the properties of dusty material in the interstellar medium (ISM), since a significant portion of its energy is emitted between ∼ 50 and 200 μm. The large-scale distribution of interstellar clouds, their thermal dust temperatures, and their column densities can be investigated with the improved spatial resolution compared to earlier all-sky survey observations. In addition to the point source distribution, the large-scale distribution of ISM cirrus emission, and its filamentary structure, are well traced. We have made the first public release of the full-sky data to provide a legacy data set for use in the astronomical community.

Key words: atlases — Galaxy: general — infrared: galaxies — ISM: general — surveys

1 Introduction

Infrared continuum emission is ubiquitous across the sky, and is attributed to the thermal emission from interstellar dust particles. These interstellar dust particles are heated by an incident stellar radiation field of UV, optical, and near-infrared wavelengths—interstellar radiation field

(ISRF)—which together have an energy peak at around 1 μm (Mathis et al. 1983). The heated dust radiates its thermal energy at longer wavelengths in the infrared to millimetre wavelength range. The spectral energy distribution (SED) of the dust continuum emission has been observed from various astronomical objects including the diffuse interstellar medium (ISM), star-formation regions, and galaxies. The observed SEDs show their peak at far-infrared (FIR) wavelength (30–300 μm), with approximately two thirds of the energy being radiated at $\lambda \geq 50$ μm (Draine 2003; also see Compiègne et al. 2011). It is thus important to measure the total FIR continuum emission energy as it is a good tracer of total stellar radiation energy, which is dominated by the radiation from young OB-stars, and thus a good indicator of the star-formation activity (Kennicutt 1998).

The first all-sky survey of infrared continuum between 12 and 100 μm was pioneered by the IRAS satellite (Neugebauer et al. 1984). It carried out a photometric survey with two FIR photometric bands centred at 60 μm and 100 μm, achieving a spatial resolution of $\sim 4'$. The IRAS observation was designed to detect point sources, but not to undertake absolute photometry (Beichman et al. 1988), leaving the surface brightness of diffuse emission with spatial scales larger than $\sim 5'$ to be measured only relatively. It has, however, been possible to create large-area sky maps (the IRAS Sky Survey Atlas: ISSA; Wheelock et al. 1994), by filtering out detector sensitivity drifts. An improvement on the efficacy of the IRAS diffuse emission data was made by combining absolute photometry data with lower spatial resolution from COBE/DIRBE observations (Boggess et al. 1992; Hauser et al. 1998), and by using an improved image destriping technique (Improved Reprocessing of the IRAS Survey: IRIS; Miville-Deschênes & Lagache 2005). An all-sky survey at submillimetre (submm) wavelengths from 350 μm–10 mm was made by the Planck satellite with an angular resolution from $5'$ to $33'$ (Planck Collaboration 2014a).

The observed FIR dust continuum SEDs are reasonably well fitted with modified blackbody spectra that have spectral indices $\beta \sim 1.5$–2, with temperatures ~ 15–20 K (Boulanger et al. 1996; Lagache et al. 1998; Draine 2003; Roy et al. 2010; Planck Collaboration 2011; Planck Collaboration 2014b; Meisner & Finkbeiner 2015). Dust particles with relatively larger sizes (big grains: BG; $a \geq 0.01$ μm with a typical size of $a \sim 0.1$ μm) are considered to be the main source of this FIR emission (Désert et al. 1990; Mathis 1990; Draine & Li 2007; Compiègne et al. 2011). The BGs are in thermal equilibrium with the ambient ISRF and thus their temperatures (T_{BG}) trace the local ISRF intensity (I_{ISRF}; Compiègne et al. 2010; Bernard et al. 2010). Measuring the SED of the BG emitters both above, and below, the peak

of the SED, is therefore important for determining T_{BG}. For the diffuse ISM, we can assume a uniform T_{BG} along the line of sight and thus can convert the observed T_{BG} to I_{ISRF}.

The opacity of the BGs (τ_{BG}) of the diffuse clouds can be evaluated from the observed FIR intensity and T_{BG}. Assuming that dust and gas are well mixed in interstellar space, τ_{BG} is a good tracer of the total gas column density including all the interstellar components: atomic, molecular, and ionized gas (e.g., Boulanger & Perault 1988; Joncas et al. 1992; Boulanger et al. 1996; Bernard et al. 1999; Lagache et al. 2000; Miville-Deschênes et al. 2007; Planck Collaboration 2011). It is also important to use estimates of τ_{BG} as a proxy to infer the foreground to the cosmic microwave background (CMB) emission that is observed in longer wavelengths (Schlegel et al. 1998; Miville-Deschênes & Lagache 2005; Compiègne et al. 2011; Planck Collaboration 2014a, 2014b; Meisner & Finkbeiner 2015).

Since the IRAS observations cover only the wavelengths at, or shorter than, 100 μm, it is important to note that emission from stochastically heated smaller dust grains becomes significant at shorter wavelengths. Compiègne et al. (2010) estimated the contribution of smaller dust emission to their observations with the PACS instrument (Poglitsch et al. 2010) onboard the Herschel satellite (Pilbratt et al. 2010) based on their adopted dust model (Compiègne et al. 2011). They estimated the contribution to be up to $\sim 50\%$ in the 70 μm band, $\sim 17\%$ in the 100 μm band, and up to $\sim 7\%$ in the 160 μm band, and concluded that photometric observations at ≤ 70 μm should be modelled by taking into account the significant contribution of emission from stochastically heated grains. To make accurate T_{BG} determination without suffering effects from the excess emission from stochastically heated smaller dust grains, the IRAS data thus need to be combined with longer wavelength COBE/DIRBE or Planck data (Schlegel et al. 1998; Planck Collaboration 2014b; Meisner & Finkbeiner 2015) or to be fitted with a modelled SED of the dust continuum (Planck Collaboration 2014c). However, COBE/DIRBE data have limited spatial resolution of a $0°.7 \times 0°.7$ field-of-view (Hauser et al. 1998). Planck data have a spatial resolution that is comparable with that of IRAS, but the data do not cover the peak of the dust SED. Observations that cover the peak wavelength of the BG thermal emission with higher spatial resolutions are therefore required.

The ubiquitous distribution of diffuse infrared emission (cirrus emission) was first discovered by IRAS observations (Low et al. 1984). Satellite and balloon observations have revealed that the cirrus emission has no characteristic spatial scales, and is well represented by Gaussian random fields with a power-law spectrum $\propto k^{-3.0}$ (Gautier et al.

1992; Kiss et al. 2001, 2003; Miville-Deschênes et al. 2002, 2007; Jeong et al. 2005; Roy et al. 2010), down to sub-arcminute scales (Miville-Deschênes et al. 2010; Martin et al. 2010). Recently, observations with Herschel with a high spatial resolution ($12''$–$18''$ at 70, 100, 160, and 250 μm) resolved cirrus spatial structures in nearby star-forming regions, showing that they were dominated by filamentary structures. These filament structures have shown typical widths of ~ 0.1 pc, which is common for all the filaments of those observed in the nearby Gould Belt clouds (cf. Arzoumanian et al. 2011; see also Arzoumanian et al. 2013 and a comprehensive review by André 2015). Prestellar cores are observed to be concentrated on the filaments (Könyves et al. 2010; André et al. 2010), suggesting that the filamentary structure plays a prominent role in the star formation process (André et al. 2014). To reveal the mechanism of the very first stages of the star formation process, the spatial scale of which changes from that of giant molecular clouds (≥ 100 pc) to the pre-stellar cores (≤ 0.1 pc), a wider field survey with a high spatial resolution is required so that we can investigate the distribution of the cirrus emission across a broad range of spatial scales, to study its nature in more detail, so as to remove its contribution as a foreground to the CMB.

For these reasons described above, we have performed a new all-sky survey with an infrared astronomical satellite AKARI (Murakami et al. 2007). The sky coverage of this survey was 99%, with 97% of the sky covered with multiple scans. The observed wavelength spans 50–180 μm continuously with four photometric bands, centred at 65 μm, 90 μm, 140 μm, and 160 μm, which have spatial resolutions of $1'$–$1'.5$. The detection limit of the four bands reaches 2.5–16 MJy sr^{-1} with relative accuracy of < 20%.

In this paper, we describe the details of the observation and the data analysis procedure. We also discuss the suitability of the data to measure the SED and estimate the spectral peak of the dust emission (so as to investigate the total FIR emission energy), and to determine the spatial distribution of the interstellar matter and star-formation activity at a high spatial resolution.

In section 2, we describe the observation made with our FIR instrument aboard AKARI. The details of the data analysis are given in section 3, including subtraction of foreground zodiacal emission, the correction scheme of transient response of FIR detectors, and image destriping. Characteristics of the produced images and their quality are described in section 4. In section 5, we describe the capability of the AKARI image to make the detailed evaluation of the spatial distribution and the SED of the interstellar dust emission. The caveats that we have about remaining artefacts in the images, and our future plans to mitigate

the effects of these, are described in section 6. Information on the data release is given in section 7. In section 8, we summarize the results.

2 Observation

We performed an all-sky survey observation with the AKARI satellite, a dedicated satellite for infrared astronomical observations (Murakami et al. 2007). Its telescope mirror had a diameter of $\phi = 685$ mm and was capable of observing across the 2–180 μm near-infrared (NIR) to FIR spectral regions, with two focal-plane instruments (FPIs): the InfraRed Camera (IRC: Onaka et al. 2007) and the Far-Infrared Surveyor (FIS: Kawada et al. 2007). Both of the FPIs, as well as the telescope, were cooled down to 6 K with liquid helium cryogen and mechanical double-stage Stirling coolers as a support (Nakagawa et al. 2007), reducing the instrumental thermal emission. The satellite was launched in 2006 February and the all-sky survey was performed during the period 2006 April–2007 August, which was the cold operational phase of the satellite with liquid helium cryogen.

The satellite was launched into a Sun-synchronous polar orbit with an altitude of 700 km, an inclination angle of $98°.2$, and an orbital period of 98 min, so that the satellite revolved along the day–night boundary of the Earth. During the survey observations, the pointing direction of the telescope was kept orthogonal to the Sun–Earth direction and was kept away from the centre of the Earth. Consequently, the radiative heat input from the Sun to the satellite was kept constant and that from the Earth was minimized (see figure 4 of Murakami et al. 2007).

With this orbital configuration, the AKARI telescope continuously scanned the sky along the great circle with a constant scan speed of $3'.6$ s^{-1}. Due to the yearly revolution of the Earth, the scan direction is shifted $\sim 4'$ per satellite revolution in a longitudinal direction or in the cross-scan direction. Consequently it was possible to survey the whole sky during each six-month period of continuous observation.

Dedicated pointed observations of specific astronomical objects were interspersed with survey observations (Murakami et al. 2007). The survey observation was halted for 30 minutes during a pointed observation to allow for 10 minutes of integration time as well as the satellite's attitude manoeuvre before and after the pointed observation. The regions that had been left unsurveyed due to pointed observations were rescanned at a later time during the cold operational phase.

The all-sky survey observations at FIR wavelengths were performed using the FIS instrument, which was dedicated for photometric scans and spectroscopic
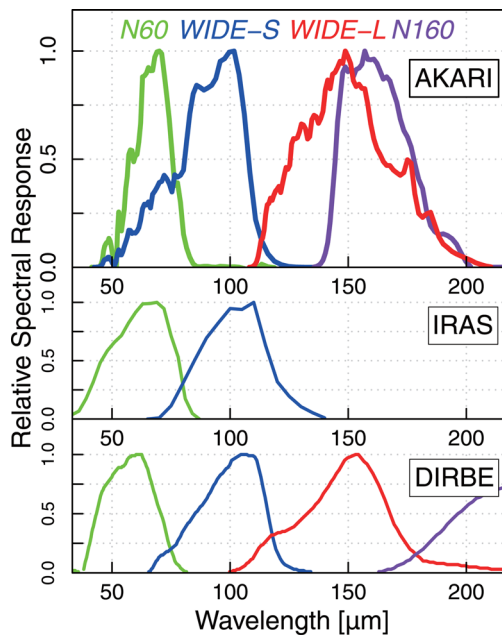
Fig. 1. Spectral responses of the four AKARI FIR bands centred at 65 μm (*N60*), 90 μm (*WIDE-S*), 140 μm (*WIDE-L*), and 160 μm (*N160*). Note that AKARI has continuous wavebands covering 50–180 μm so that we can make a precise evaluation of the total FIR intensity from the in-band flux of the AKARI observations. Spectral responses of IRAS and COBE/DIRBE are also shown for comparison. (Colour online)

observations across the 50–180 μm spectral region (Kawada et al. 2007). Four photometric bands were used for the all-sky survey. The spectral responses of the bands are shown in figure 1 and the characteristics of the bands are summarized in table 1. Two of the four bands had a broader wavelength coverage and continuously covered the whole waveband range: the *WIDE-S* band (50–110 μm, centred at 90 μm) and the *WIDE-L* band (110–180 μm, centred at 140 μm). The two other bands had narrower wavelength coverage and sampled both the shorter and the longer ends of the wavebands: the *N60* band (50–80 μm, centered at 65 μm) and the *N160* band (140–180 μm, centered at 160 μm).

The pixel scales of the detectors were $26''.8 \times 26''.8$ for the short wavelength bands (*N60* and *WIDE-S*) and $44''.2 \times 44''.2$ for the long wavelength bands (*WIDE-L* and

N160; table 1). The cross-scan widths of the detector arrays were $\sim 8'$ for *N60* and *WIDE-S* and $\sim 12'$ for *WIDE-L* and *N160* (see figure 3 of Kawada et al. 2007). These array widths corresponded to two or three times the shift of the scan direction per satellite revolution ($\sim 4'$, see above). With a continuous survey observation, as a result, regions close to the ecliptic plane were surveyed at least twice with the *N60* and *WIDE-S* bands and three times with the *WIDE-L* and *N160* bands. Regions at higher ecliptic latitudes had increasingly greater exposure times and numbers of confirmatory scans.

The detector signals were read out by Capacitive Trans-Impedance Amplifiers (CTIAs) that were specially developed for this satellite mission (Nagata et al. 2004). The CTIA is an integrating amplifier that allows the detector signal to be read out as an integration ramp, with a slope that is proportional to the detector flux. The signal level was sampled at 25.28 Hz (*N60*, *WIDE-S*) and 16.86 Hz (*WIDE-L*, *N160*), which corresponded to about three samples in a pixel crossing time of an astronomical source (Kawada et al. 2007).

The integrated electrical charge was reset periodically so that the output voltage remained well within the dynamic range of the CTIA. We applied regular reset intervals of either 2 s, 1 s, or after every sampling (correlated double sampling: CDS) for the all-sky survey observations depending upon the sky brightness, with reference to the sky brightness at 140 μm observed with COBE/DIRBE from the Annual Average Map (Hauser et al. 1998). A reset interval of 2 s was normally applied, although it was shortened to 1 s for the brighter celestial regions with > 60 MJy sr^{-1}. The CDS mode was applied for sky with > 210 MJy sr^{-1}, which mainly corresponds to the inner Galactic plane.

An additional calibration sequence was periodically carried out during the survey observations to calibrate the absolute and relative sensitivities of the various detector channels. The FIS was equipped with a cold shutter to allow absolute sensitivity calibration (Kawada et al. 2007). The shutter was closed for one minute after every 150 minutes of observations, or after ~ 1.5 orbits of the satellite, so as to estimate the dark-sky condition, and to measure

Table 1. Specification of the AKARI FIR detectors (Kawada et al. 2007; Shirahata et al. 2009).

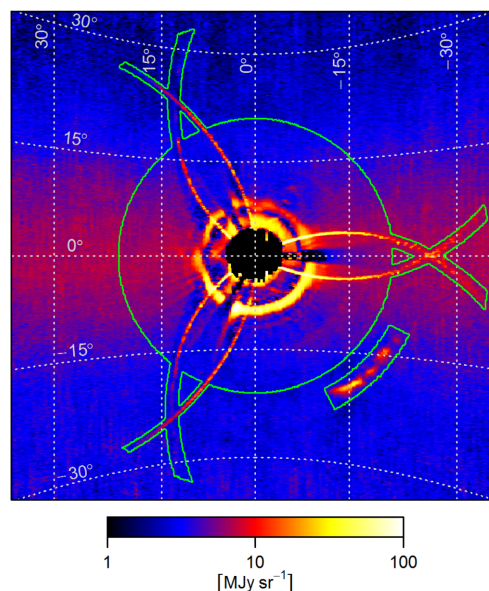| Band name	N60	WIDE-S	WIDE-L	N160	
Centre wavelength	65	90	140	160	[μm]
Wavelength range	50–80	60–110	110–180	140–180	[μm]
Array format	20 × 2	20 × 3	15 × 3	15 × 2	[pixel]
Pixel scale*	$26''.8 \times 26''.8$		$44''.2 \times 44''.2$		
Pixel pitch*	$29''.5 \times 29''.5$		$49''.1 \times 49''.1$		
Detector device	Monolithic Ge : Ga array		Stressed Ge : Ga array		

*At the array centre.
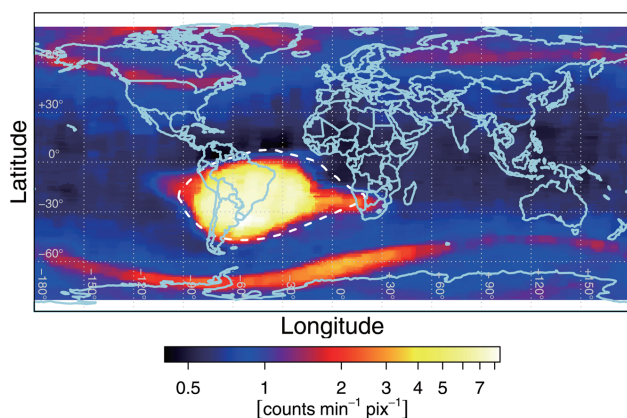
Fig. 2. Spatial distribution of the high-energy particle hit rate evaluated from in-flight data of the FIS detector signal. The dashed line indicates the region where we stopped the FIS observation during the satellite passages. (Colour online)

Fig. 3. Scattered light around the Moon observed in the *WIDE-L* band. The Moon's position is at the centre of the figure. We closed the shutter near the Moon $< 5°$ and thus no data are available at the region around the Moon. The broad diffuse horizontal feature in the middle of the figure is the zodiacal dust band component, which has not been removed from the data (see subsection 3.2). The solid lines indicate the regions which are contaminated by the scattered light. The data observed in these regions were eliminated from the image processing. (Colour online)

the absolute zero level of the detector signal. A constant illumination calibration flash was also applied for 30 seconds while the shutter was closed so that we could calibrate the responsiveness of the detector channels in addition to the dark measurement. This calibration sequence was performed when the regions near the north or the south ecliptic pole were surveyed as the regions were repeatedly surveyed with many survey scans. The observed regions that were affected by this calibration sequence were intentionally scattered in the pole regions so that we could maximize the on-sky observing time.

In addition to the absolute calibration sequences mentioned above, a calibration light was flashed every minute during the survey observations to calibrate sensitivity drifts whose time variations were shorter than 150 minutes. The flash simulated the profile of a point source crossing the field of view (FOV) of each detector pixel.

High-energy particles hitting the detector cause glitches or sudden jumps in the detector signals (Suzuki et al. 2008), which must be restored or removed from analyses to eliminate false detection of astronomical objects. However, the high frequency of high-energy particle hits prevents continuous observations, and may even cause significant drift of the detector responsiveness. A region above the Earth's surface over the South Atlantic is known to have anomalous geomagnetic field which leads to a higher density of solar protons (the South Atlantic Anomaly: SAA). We characterized this region from in-flight data of particle hit rates as shown in figure 2. We paused the survey observation during satellite passages through this region.

During the SAA passages, the response of each detector pixel was significantly changed due to high frequency hitting of high-energy particles, which led to the excitation

of charged particles in the detector material (Suzuki et al. 2008). To restore the detector responsivity, we applied a high electrical voltage (of the order of 1 V) for 30 seconds to each detector pixel to flush out the charged particles (bias-boosting). We performed a bias-boost operation after every SAA passage, waiting for one minute after exiting from the SAA region, and restarting the survey observations two minutes later after the bias-boost procedure.

The scattered light of bright objects from the telescope structures at the periphery of the telescope's FOV can also affect the survey data, and emission from the Moon was found to be the dominant contributor to this contamination. Thus we measured the scattered light pattern as shown in the figure 3 and eliminated the contaminated data from the image processing (section 3). The eliminated region is indicated in figure 3 with the solid lines. The scattered light from bright planets (Jupiter and Saturn) also needs to be considered, but we have not currently applied a correction for these signals, and will defer this to a later reprocessing of the image data (subsection 6.2).

Interruption of the survey observations due to SAA passages, interference from the Moon, and pointed observations left gaps in the sky coverage in the first six months' survey coverage. These gaps were filled in later using AKARI's attitude control, which allowed cross-scan offsets $< \pm 1°$.

Ecliptic Coordinates

Equatorial Coordinates

Galactic Coordinates

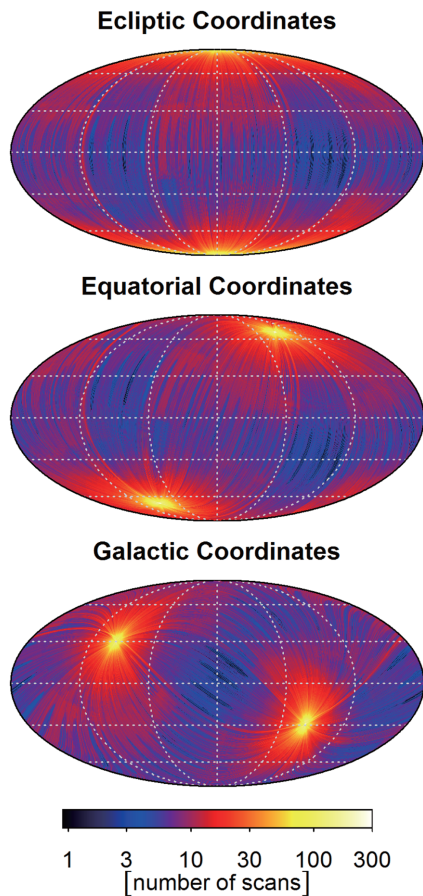1 3 10 30 100 300
[number of scans]

Fig. 4. Sky coverage of the AKARI all-sky survey. Spatial scan numbers are displayed in different celestial coordinates. (Colour online)

A summary of the survey coverage and completeness is shown in figure 4 and table 2. After about 17 months of the survey period (the cold operational phase), 97% of the sky was multiply surveyed in the four photometric bands.

3 Data analysis

The data obtained during the observations were pre-processed using the AKARI pipeline tool originally optimized for point source extraction (Yamamura et al. 2009). This included corrections for the linearity of the CTIAs and sensitivity drifts of the detectors referenced against the calibration signals (section 2), rejection of anomalous data

due to high-energy particles (glitches), signal saturation, and other instrumental effects as well as dark-current subtraction (Kawada et al. 2007; Yamamura et al. 2009). The orientation of the detector FOV was determined using data taken with NIR star cameras (Yamamura et al. 2009).

Following this initial preprocessing, a separate pipeline was then used to accurately recover the large-scale spatial structures. The main properties of the diffuse mapping pipeline are as follows: (1) transient response correction of the detector signal, (2) subtraction of zodiacal emission, (3) image processing, (4) image destriping, and (5) recursive deglitching and flat-fielding to produce the final image. Processes (1) and (2) are performed on the time-series data and (3)–(5) are performed on image plane data. In the following subsection, we describe the details of these procedures.

### 3.1 Time-series data analysis with transient response correction

The time-series signal from each detector pixel was processed to recover the true sky flux. First we eliminated anomalous data that were detected during preprocess, including glitches and data for which the output of the CTIAs became non-linear because of signal saturation. The data collected during CTIA resets and calibration lamp flashes were also removed (see section 2 for the amplifier reset and calibration lamp operation).

The data were then converted to astronomical surface brightness [MJy sr^{-1}] from the raw output signal values, multiplied by calibration conversion factors (Takita et al. 2015). Different conversion factors were applied to the data taken in the nominal integration mode and in the CDS mode (section 2), so that these data are treated separately (Takita et al. 2015).

The transient response, due to the nonlinear behaviour of the detector, is a major cause of distortion of the detector time-series signal (Kaneda et al. 2009) and its correction is particularly important for the recovery of high quality diffuse structure (Shirahata et al. 2009). Kaneda et al. (2009) have previously discussed the characterisation of detector slow-response effects and their mitigation, and we take a practical approach here to correct the all-sky survey data so

Table 2. Scan coverage of the survey observations.

Scan coverage	Covered region	Multiply covered region	≥ 5 times	≥ 10 times	Not covered
N60	99.1%	96.9%	60.3%	13.5%	0.9%
WIDE-S	99.1%	97.0%	61.0%	13.8%	0.9%
WIDE-L	99.5%	98.4%	78.7%	25.9%	0.5%
N160	99.5%	98.4%	76.8%	24.1%	0.5%
Four bands	99.1%	96.8%	60.0%	13.2%	0.9%
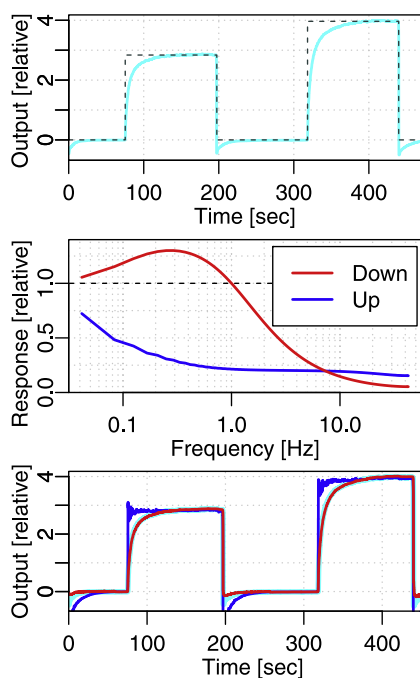
Fig. 5. Top panel: step function of the detector signal taken in-flight by an internal calibration lamp illumination. The cyan line shows the detected signal and the black broken line shows a schematic of the lamp illumination pattern. Middle panel: spectral response functions of a detector pixel. The blue line shows a spectral response that is estimated from the upward step function and the red line shows a spectral response that is estimated from the downward step function. Correction functions for the transient response of the detector are evaluated from these spectral responses (see text). Bottom panel: signal correction by the correction functions evaluated from the above spectral responses. The cyan line is the raw detector signal, which is the same signal shown in the top panel. The blue line is a corrected signal by applying the upward correction function and the red line is a corrected signal by applying the downward correction function. A reasonable signal profile is reproduced by taking the upper envelope of the two corrected signals.

that high-quality diffuse maps can be recovered with realistic computational overheads (see Doi et al. 2009 for the details of the computation scheme).

Figure 5, top panel, shows an example detector signal that was taken during an in-flight dedicated calibration sequence. The cold shutter was closed to achieve the absolute zero level (section 2), meanwhile constant illumination with internal calibration lights was performed with two different luminosities ($t = 80$–200 s and $t = 320$–440 s). The output signal should be a rectangular wave (the black broken line in the figure) if the detector had an ideal time response, while the observed signal showed significant distortion due to the transient response. Upward steps of the observed signal showed slow time responses that took several tens of seconds to reach a stable signal level. On the other hand, downward steps showed relatively quick responses with significant overshoot at the falling edges.

Since these signals are step response functions to the incident light, we can evaluate frequency response functions of the detector as the Fourier transformation of the detector signal (figure 5, middle panel). The response became low at higher frequencies due to slow-response effect of the detector. In addition to that, the downward response showed signal amplification at < 1 Hz, which corresponds to the overshoot of the detector signal.

The transient response of the raw detector signal can be corrected by multiplying the signal by the correction function, whose frequency response is the inverse of that of the detector. Thus the correction function is obtained by deriving the reciprocal of the detector frequency response and then making a Fourier inverse transformation of the reciprocal data. Since the response function for upward steps and that for downward steps were significantly different, we derived both upward and downward transient correction functions and applied both to the same detector signal (figure 5, bottom panel). A reasonable correction is achieved by taking the larger signal at each sampling, which is the upper envelope of the two corrected signals.

Since the high-frequency signal component is amplified with the transient response correction, the high-frequency noise is also amplified. To mitigate this side effect, we suppressed the high-frequency part of the numerical filtering to filter out the frequency components that had higher frequencies than the signal crossing time of the detector FOV. The residual glitch noises should be eliminated by a deglitching process described below (subsections 3.3 and 3.5). An example of the application of this transient response correction process to an actual astronomical image (M 33) is shown in figure 6.

3.2 Subtraction of zodiacal emission

The zodiacal light emission (ZE) is the thermal emission from the interplanetary dust (IPD) and the dominant diffuse radiation in the mid-infrared (MIR) to FIR wavelength regions. Since the dust around 1 au from the Sun has a thermal equilibrium temperature of ~ 280 K, the ZE has a spectral peak around 10–20 μm, and it dominates the MIR brightness in the diffuse sky. Even in the FIR, the ZE contribution is not completely negligible at high galactic latitude. Therefore the ZE component should be segregated from the observed signal to make astronomical sky maps.

Many efforts have been devoted to describing the structure of the zodiacal dust cloud. In particular, a number of models have been developed using the infrared satellite data, such as IRAS and COBE/DIRBE. The ZE model most commonly used to date is the one based on the DIRBE data (e.g., Kelsall et al. 1998; Wright 1998; hereafter the Kelsall model and the Wright model, respectively). The
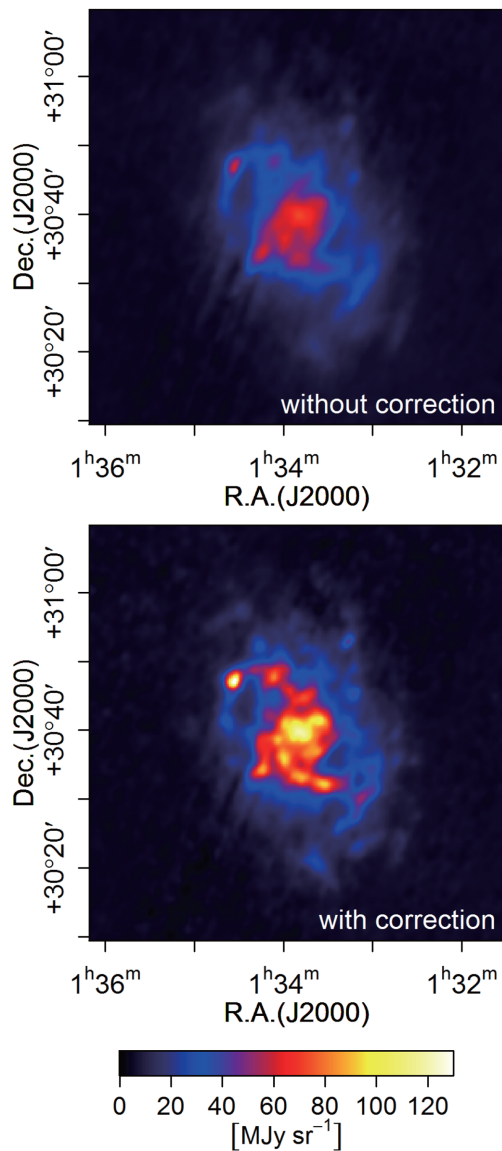
Fig. 6. Example of the transient response correction that is applied to M 33 _WIDE-L_ images. The top panel shows the image without the correction for the comparison to the image with the correction in the bottom panel. An image destriping process (subsection 3.4) has been applied for both images. (Colour online)

Kelsall and the Wright models explain the IPD cloud complex with the following three components: a smooth cloud, asteroidal dust bands, and a mean motion resonance (MMR) component. The MMR component is further divided into a circumsolar ring and a blob trailing the Earth in the Kelsall model. For each of the three components, they introduced parametrized functions to describe the spatial distribution of the dust number density in the heliocentric coordinates. Gorjian, Wright, and Chary (2000), hereafter the Gorjian model, investigated the DIRBE ZE model in depth and modified the parameters of the Wright model.

Although the most part of the ZE structure in AKARI FIR images can be well reproduced with the Kelsall or the Wright/Gorjian models, there are discrepancies at small-scale structures. In particular, the intensity and the ecliptic latitudes of the peak positions of the asteroidal dust bands cannot be precisely reproduced with these models. Pyo et al. (2010) also reported an inconsistency of 20% for the intensity of the ring component between the AKARI observations and the Kelsall model prediction in MIR. From these points of view, we only subtracted the smooth cloud component of the ZE based on the Gorjian model at this stage. The contribution of the asteroidal dust bands and the MMR component will be described in a separate paper (T. Ootsubo et al. in preparation), which will provide a ZE model including all components for AKARI FIS all-sky images.

The Gorjian model evaluates the expected ZE brightness in the DIRBE bands. Based on this model evaluation, we estimated the SED of the diffuse ZE component by interpolating the expected ZE brightness in 25, 60, 100, 140, and 240 µm DIRBE bands using a cubic Hermite spline. Then the expected diffuse ZE brightness in each AKARI band was estimated by multiplying this SED by each AKARI band (figure 1). The Earth's orbital position in the solar system at time of the observation and the viewing direction from the satellite were also considered in the model estimation to take the nonuniform spatial distribution of the IPD cloud in the solar system into account.

The intensities of dust band and MMR components remaining in the released AKARI FIR images are less than about 5 MJy sr^{-1} for all bands. Detailed values and caveats about the ZE are given in subsection 6.1.

3.3 Image processing from time-series signals

The processed time-series data described above were used to produce a preliminary intensity image. To evaluate the intensity of an individual image pixel, we selected data samples near the pixel centre. The selection radius was set at three times the half-power beamwidth (Shirahata et al. 2009; Takita et al. 2015).

Outlier data were removed from the samples. The outliers are mainly due to (1) glitch residuals, (2) noise signal amplified by the transient response correction, and (3) baseline offsets due to long-term sensitivity variations of the detector. The outliers (1) and (2) were eliminated by using a sigma clipping method, and at this level about half of the data samples were eliminated. About the outliers (3), a string of data was eliminated by identifying what had intensity distribution functions distinct from other data. These eliminated data were restored with an additional gain and offset adjustment in a later stage of the data processing (subsection 3.5).

The residual data were weighted by distance from the pixel centre by assuming a Gaussian beam profile, whose full width at half maximum was 30″ for *N60* and *WIDE-S*, and 50″ for *WIDE-L* and *N160*, so that the beam width was comparable to the spatial resolution of the photometric bands and did not therefore degrade the spatial resolutions of resultant images significantly. The weighted mean of the residual data was then taken as the preliminary intensity of the image pixel. The weighted standard deviation, sample number, and spatial scan numbers were also recorded.

3.4 Image destriping

The resultant images show residual spatial stripes due to imperfect flat-fielding caused by long-term sensitivity variations of the detector. To eliminate this artificial pattern, we developed a destriping method based on Miville-Deschênes and Lagache (2005), who developed their destriping method to obtain the IRIS map. The details of our procedure will be described in M. Tanaka et al. (in preparation). We describe a brief summary in this paper.

The destriping method by Miville-Deschênes and Lagache (2005) can be summarized as follows.

(i) Image decomposition: an input image is decomposed into three components (a large-scale emission map, a small-scale emission map, and a point-source map).

(ii) Stripe cleaning: the small-scale emission map is Fourier-transformed to obtain a spatial frequency map. Spatial frequency components that are affected by the stripes are confined in the spatial frequency map along the radial directions that correspond to the stripe directions in the original intensity map. The affected spatial frequency components are replaced with magnitudes that have averaged values along the azimuthal direction (see figure 1 of Miville-Deschênes & Lagache 2005).

(iii) Image restoration: the stripe-cleaned map is inversely Fourier-transformed and combined with the other decomposed images (a large-scale emission map and a point-source map).

We find that the stripe cleaning process of the small-scale emission map described above causes strong spurious patterns in some of the resultant images containing bright molecular clouds (e.g., Orion clouds). This is because such regions contain small-scale and large-amplitude fluctuations of emission, which leads to contamination of the derived spatial spectrum over the spatial frequency domain. In this case, the subsequent destriping process unexpectedly modifies the contaminated components of the spatial spectrum and causes artefact patterns. Therefore, we masked the regions that showed large intensity variance in a small-scale map and eliminated those regions from the stripe cleaning
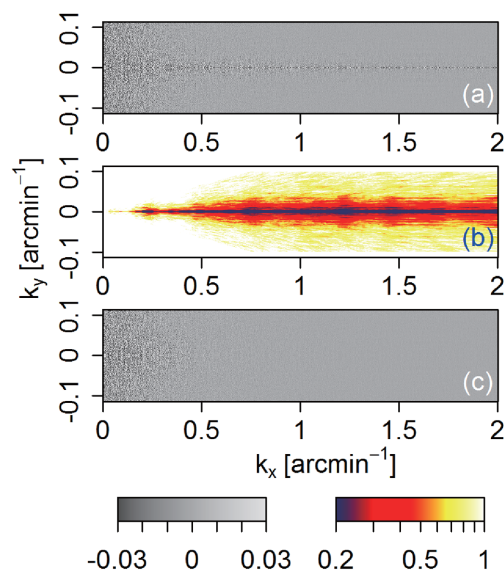
Fig. 7. (a) Spatial frequency map before destripe, obtained with Fourier transformation of an original intensity map containing stripe noises. The real part of the complex Fourier moduli is plotted for panels (a) and (c). (b) Map of an attenuation factor, $A(r, \theta)$. See text for the definition of $A(r, \theta)$. (c) Destriped spatial frequency map, obtained by multiplying (a) by (b). We show details of the maps around the x-axis ($x \geq 0$ arcmin^{-1}, $|y| \leq 0.11$ arcmin^{-1}), as the excess component caused by the stripe noises is confined along the x-axis (see text). The colour scales of the images are from −0.03 to 0.03 on linear scale for (a) and (c) and from 0.2 to 1.0 on logarithmic scale for (b). Colour bars are shown at the bottom of the figure. (Colour online)

process, in addition to a large-scale emission map and a point-source map. As an indicator of the variance, we calculated the local root mean square (rms) of the pixel values on a small-scale map and eliminated the regions whose local rms was greater than a threshold value ($2 \times$ rms of entire region). We need to apodize the discontinuity of pixel values at the boundaries of the eliminated regions to suppress spurious spectrum patterns in the estimated spatial frequency spectrum. Thus we multiplied the pixel values in the eliminated regions by $[1 + (s - 1)^2]^{-1}$, where s is (local rms)/threshold, instead of filling the regions with zero.

The derived small-scale map was then Fourier-transformed to obtain a two-dimensional spatial frequency map. We applied the stripe cleaning process to the images in ecliptic coordinates, in which the scanning direction of the AKARI survey is parallel to the y-axis of the images (see section 2 for the spatial scan during the all-sky survey observations). This is beneficial because the direction of the spatial stripe patterns caused by the spatial scans become parallel to the y-axis, then noises caused by the stripes are confined along the x-axis of the two-dimensional spatial frequency map as shown in figure 7a. The stripe cleaning can be achieved by suppressing the power excess along the x-axis. While Miville-Deschênes and Lagache (2005) made substitution of the pixel values in their noise-contaminated

regions with the azimuthal-averaged values, we multiplied the spatial frequency map by an attenuation factor $A(k)$, where k is a wavenumber vector, to suppress the power excess. This attenuation factor is similar to a filter in signal processing, which is used for converting an input spectrum $F(k)$ to an output spectrum $G(k) = A(k)F(k)$. Since a discontinuous filter function, such as a box-car function, causes ripples on the result of Fourier transform, a smooth function is better for suppressing artefact. Therefore, we calculated the attenuation factor as follows. First we obtained a power spectrum $P(r, \theta)$, where (r, θ) is a position on the two-dimensional spatial frequency map in the polar coordinate system. Next, we calculated the azimuthal average of $P(r, \theta)$ as $\bar{P}_a(r)$, where a region around the x-axis was excluded from the averaging. Then, we calculated the local average of $P(r, \theta)$ as $\bar{P}_l(r, \theta)$, in the range of $r \pm \sqrt{r}/2$ pixels along the radial direction of the spatial frequency map. Finally, the attenuation factor was calculated as

$$A(r, \theta) = \begin{cases} [\bar{P}_a(r)/\bar{P}_l(r, \theta)]^{\frac{1}{2}} & \text{(if } \bar{P}_l(r, \theta) > \bar{P}_a(r) \\ & \text{and } (r, \theta) \in R_A) \\ 1 & \text{(otherwise)} \end{cases} \quad (1)$$

where R_A is a region around the x-axis defined by a particular range in θ and y. Figure 7b shows an attenuation factor map obtained for a two-dimensional spatial frequency map shown in figure 7a. Since $\bar{P}_l(r, \theta)$ is the local average of $P(r, \theta)$, $A(r, \theta)$ has smooth distribution in the radial direction. Figure 7b also shows that $A(r, \theta)$ is close to unity if $|y| > 0.05$ arcmin^{-1}, which means that our destripe process is not sensitive to the definition of R_A. The resultant destriped spatial frequency map is shown in figure 7c, which is obtained by multiplying the spatial frequency map (a) by the attenuation factor (b). The result shows that the spatial frequency is attenuated down to the level of the azimuthal average.

We tested our destriping method in a similar way to Miville-Deschênes and Lagache (2005), using simulated images composed of the ISM with a spectral power-law index of $\gamma = -3$ as well as random and stripe noises. The result is shown in figure 8. Our simulation shows that our method does not modify the power spectrum by more than 1% at small scale.

3.5 Recursive deglitching and flat-fielding by referring to the processed image

Stripes were eliminated from the preliminary image by the above-mentioned process, which was a consequence of long-term sensitivity drift of the detectors. To restore those data and to perform better deglitching, we reprocessed the time-series data by referring to the preliminary image.
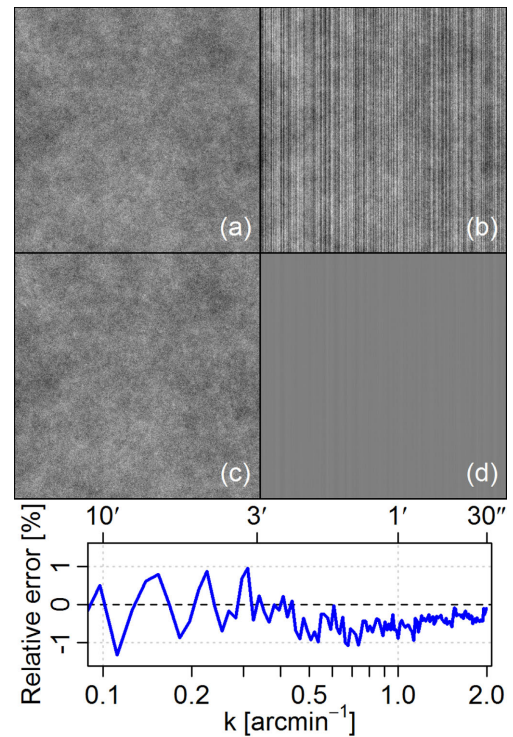
Fig. 8. A verification of the image restoration with our destriping method. (a) Synthetic image of ISM with random noise. (b) Input image for destriping made by adding stripe noises to (a). (c) Destriped image. (d) Residual error of (c) minus (a). The colour scales are the same for the four images. Bottom panel: relative error between the spatial spectra of (c) and (a) derived by [(c) − (a)]/(a). (Colour online)

An additional gain and offset adjustment was made for each set of time-series data by each detector pixel to get better correction of the flat-fielding, by fitting each set to the preliminary image. At the same time, outlier data rejection was also made by eliminating the data that exceeded 10 times the standard deviation from the reference image.

The final image was then processed by using the time-series data and was cleaned by the image destriping process described above.

We processed the whole sky image in $6° \times 6°$ image patches with $5°$ separations. These processed images were then combined into larger images using the Montage software package (Berriman et al. 2008).

4 Results

Intensity maps from the all-sky survey in the four photometric bands are shown in figure 9. Detailed photometry with high spatial resolution has been achieved for the whole sky. The FIR intensity distribution of the emission shows a clear wavelength dependence, concentrated more at the Galactic plane at shorter wavelengths and with significant extension towards higher galactic latitudes being seen at longer wavelengths. The concentration at the Galactic plane
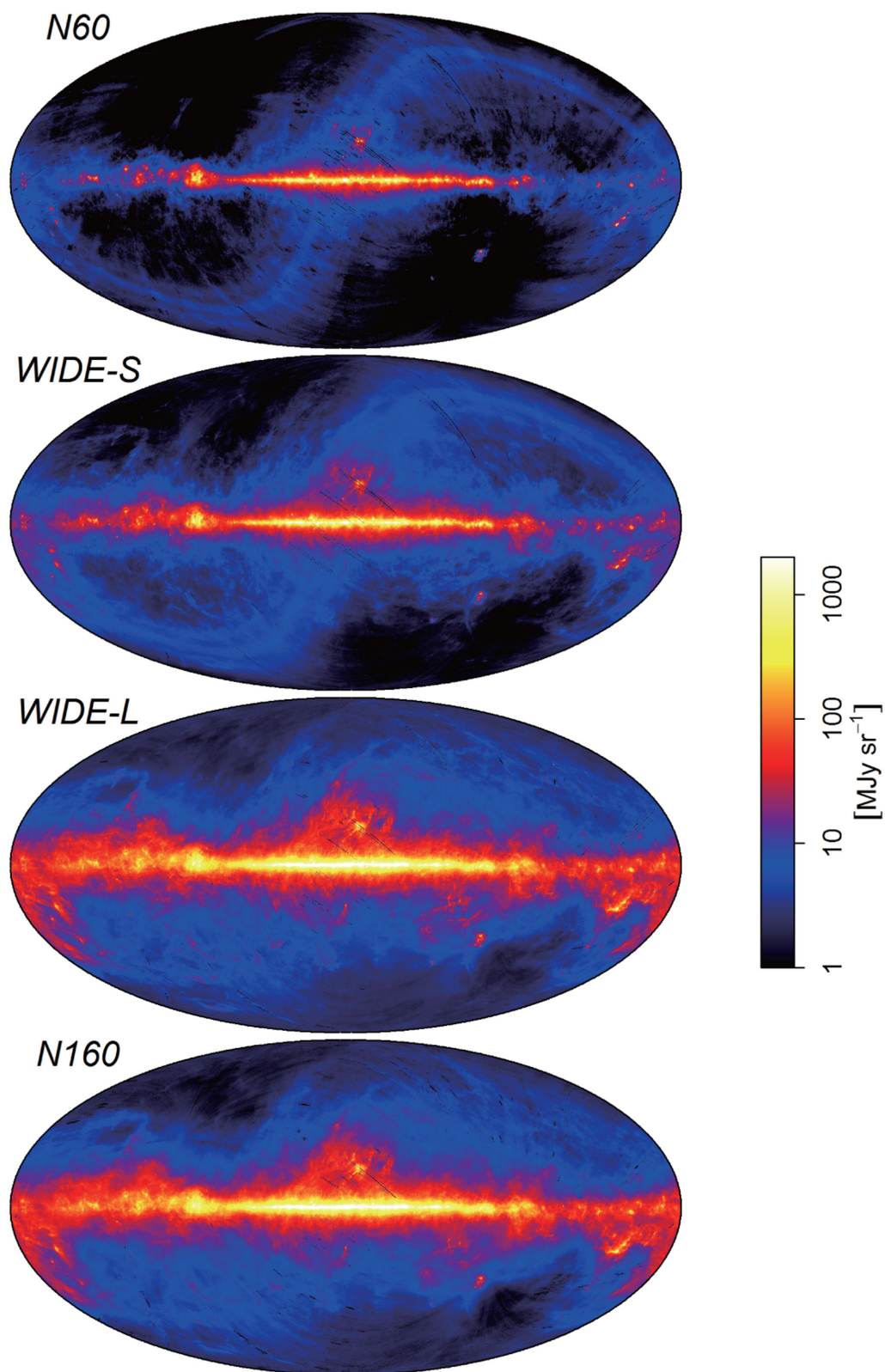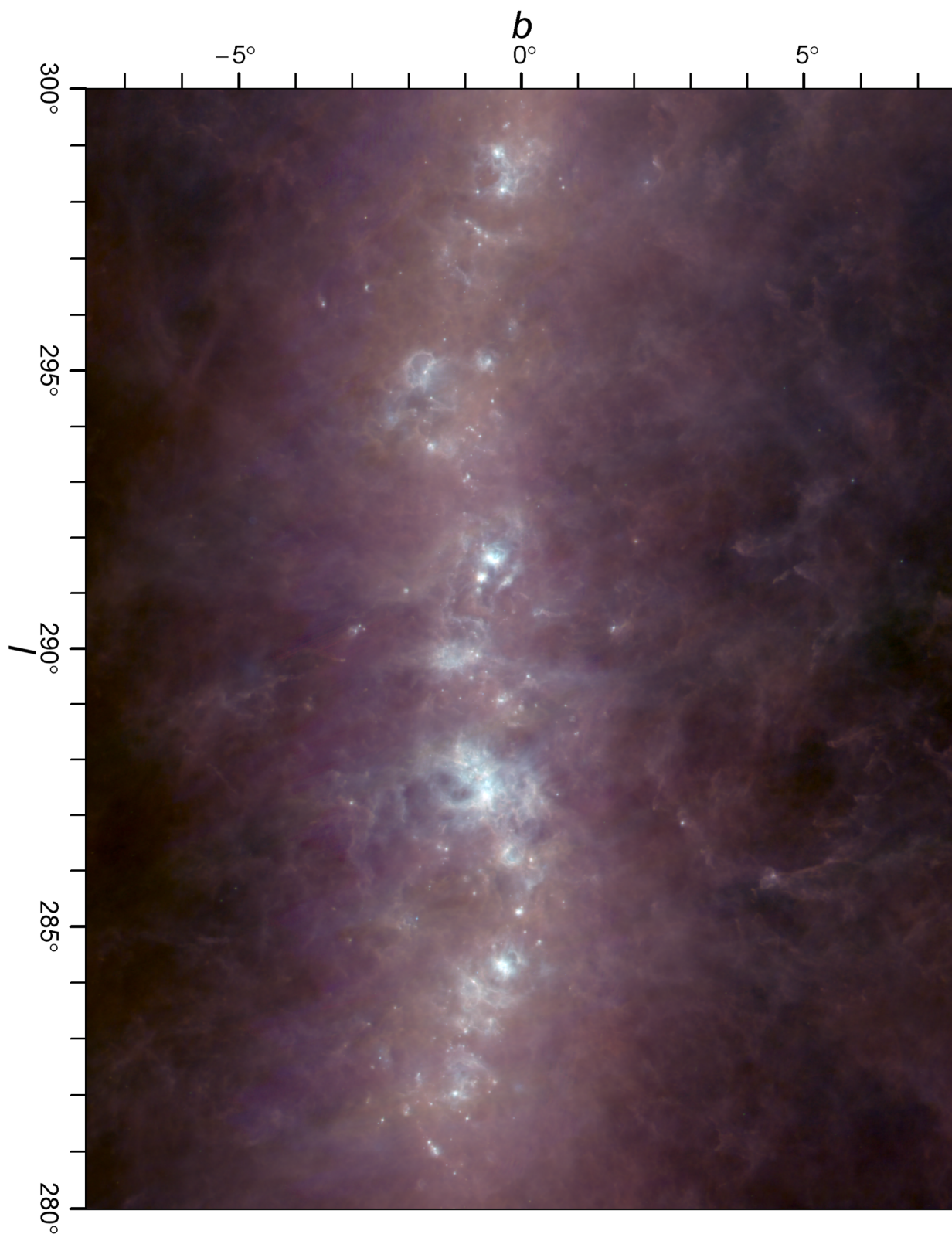
Fig. 9. All-sky FIR intensity maps observed by the AKARI survey.

Fig. 10. Three-colour composite image of the Galactic plane around η Carinae region. *N60* (blue), *WIDE-S* (green), and *WIDE-L* (red) images are combined. Intensities are from 1 to 10000 MJy sr^{-1} on logarithmic scale.

indicates a tighter connection to the star-formation activity by tracing high ISRF regions at and around star-forming regions. The extended emission seen at longer wavelengths traces spatial distribution of low-temperature dust in high-latitude cirrus clouds. This noticeable dependence of the spatial distribution on the wavelength difference between 65 μm and 160 μm shows the importance of the wide wave-length coverage of AKARI to observe the FIR dust emission at the peak of its SED where it has the largest dependence on the temperature difference of the dust particles. This difference in concentration at the Galactic plane is also visible in a zoomed-in image of the Galactic plane at $l = 280°$–$300°$ (figure 10).

The emission ranging from the tenuous dust in high Galactic cirrus clouds to the bright inner Galactic plane has been successfully measured in the AKARI all-sky images. A companion paper (Takita et al. 2015) describes further details of the data calibration and the reliability estimation, and confirms that a good linearity correction has been achieved for all the bands, from the faintest detector signals up to the bright signals of > 10 GJy sr^{-1}, with relative accuracy of $\sim 10\%$. It is important to note that the good linearity correction achieved for the data also confirms the successful correction of the spatial distortion of the data caused by the transient response of the detector. The intensity calibration is done primarily by using more sensitive slow-scan data (Shirahata et al. 2009), and the linearity and absolute intensity have been checked with IRAS/IRIS (Miville-Deschênes & Lagache 2005) and COBE/DIRBE (Hauser et al. 1998). Takita et al. (2015) estimates that an absolute accuracy of 20% has been achieved for all the bands with intensities of ≥ 6 MJy sr^{-1} for $N60$, ≥ 2 MJy sr^{-1} for $WIDE\text{-}S$, and ≥ 15 MJy sr^{-1} for $WIDE\text{-}L$ and $N160$. The better absolute accuracy has been achieved for brighter regions, and that of 10% has been achieved for ≥ 10 MJy sr^{-1} for $N60$, ≥ 3 MJy sr^{-1} for $WIDE\text{-}S$, ≥ 25 MJy sr^{-1} for $WIDE\text{-}L$, and ≥ 26 MJy sr^{-1} for $N160$. Takita et al. (2015) also estimates the full width at half maximum of the point spread function $63''$, $78''$, and $88''$ for $N60$, $WIDE\text{-}S$, and $WIDE\text{-}L$, respectively. Although no evaluation of the point spread function is available for $N160$ due to the lower sensitivity of the $N160$ band (Takita et al. 2015), a comparable point spread function is expected for $N160$ the same as for $WIDE\text{-}L$ since they are comparable in the more sensitive slow-scan data (Shirahata et al. 2009). Improvement of the spatial resolution compared to IRAS images is demonstrated in figure 11.

The residual of the ZE along the ecliptic plane is visible in shorter wavelength images, especially in the $N60$ image. This is because we have subtracted the spatially smooth component from the data but have not subtracted the dust band component, which has smaller scale structures that
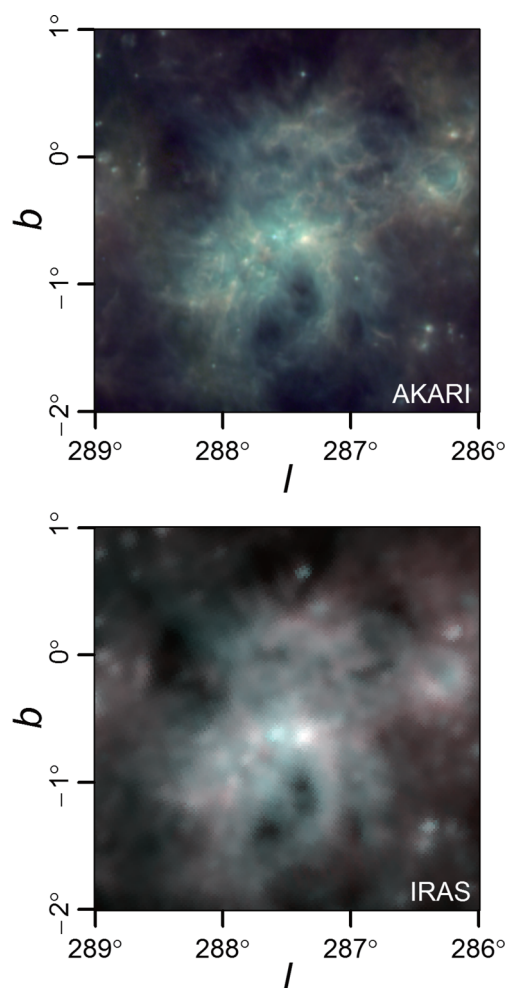

Fig. 11. Zoomed-in images of the η Carinae region. Upper panel: three-colour composite of $N60$ (blue), $WIDE\text{-}S$ (green), and $WIDE\text{-}L$ (red) images. Lower panel: composite image of IRIS 60 μm (cyan) and IRIS 100 μm (red) images for a comparison of spatial resolutions between IRAS and AKARI images.

are for the first time revealed by the high spatial resolution AKARI observation (subsection 3.2). The former models of the ZE cannot reproduce this spatial distribution properly, so we need to develop our own model to remove the emission from the celestial image. Our current estimation of the ZE is briefly described in subsection 6.1 and will be investigated in detail in a future paper (T. Ootsubo et al. in preparation).

5 Discussion

5.1 Spatial power spectra

Our survey images are the first-ever FIR images that cover the whole sky with arcmin spatial resolution. A major advantage of the AKARI data is that it enables us to obtain the global distribution of the ISM with higher spatial resolutions. In other words, the large spatial dynamic range of
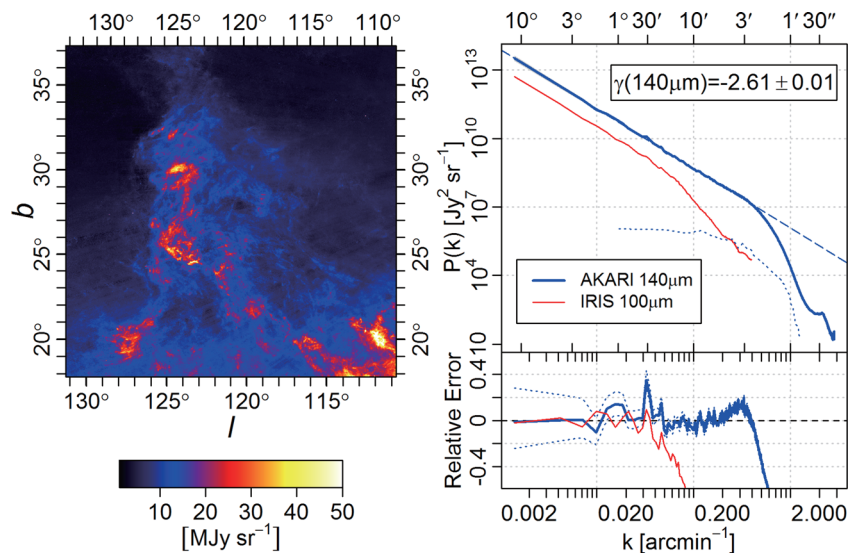
Fig. 12. Left-hand panel: *WIDE-L* intensity image of the Polaris flare region. Right-hand upper panel: spatial power spectrum of *WIDE-L* intensity (the blue solid line) observed in the Polaris flare region shown in the left-hand panel. A power-law fitting of the spectrum at the scales of $0.0014 < k < 0.21$ arcmin^{-1} is shown as the blue dashed line with a power index of -2.61 ± 0.01. The blue dotted line shows the spectrum of the point spread function, which is arbitrarily shifted in the vertical direction by comparison with the *WIDE-L* power spectrum. The red solid line shows the spatial spectrum of the IRIS 100 μm data of the same region for comparison. Right-hand lower panel: relative error of *WIDE-L* spatial spectrum from the power-law fitting shown in the right-hand upper panel (the blue solid line). Standard error of the *WIDE-L* spatial spectrum estimation is denoted as the blue dotted line. The relative error of the IRIS 100 μm data is also shown as the red solid line for comparison.

the data is one of the key characteristics of the AKARI FIR survey. This characteristic can be examined by calculating the spatial power spectra of the cirrus distribution taken from the AKARI all-sky survey, as the cirrus power spectra can be well represented by power-law spectra (section 1).

Miville-Deschênes et al. (2010) derived the IRAS/IRIS 100 μm and Herschel/SPIRE 250 μm combined spatial power spectrum at the Polaris flare region and confirmed that the power-law nature of the cirrus power spectrum is kept down to sub-arcmin scales, with a power-law index $\gamma = -2.65 \pm 0.10$ on scales $0.025 < k < 2$ arcmin^{-1} (also see Martin et al. 2010). Since the Polaris flare is a high galactic latitude cirrus cloud with virtually no sign of star-formation activity (Ward-Thompson et al. 2010; Martin et al. 2010), the region is well suited to assessing the nature of the cirrus power spectrum.

The AKARI FIR image of the Polaris flare region and its spatial power spectra are shown in figure 12 (also see Doi et al. 2012).

Good linearity is found from a small scale of $\sim 3'$ to the larger scales beyond $10°$, which is consistent with the measurements of many other authors (Miville-Deschênes et al. 2010 and the references therein). The power-law index is estimated $\gamma_{140\,\mu m} = -2.61 \pm 0.01$ by fitting the *WIDE-L* 140 μm spectrum in a $k = 0.0014$–0.21 arcmin^{-1} wavenumber range. An excess component from the fitted power-law spectrum is found in the wavenumber range ~ 0.2–0.4 arcmin^{-1} (the right-hand lower panel of

figure 12; see also figure 3 of Doi et al. 2012), which is due to the noise in the data. Thus we limit the wavenumber range for the fit as < 0.21 arcmin^{-1} and eliminate all the data above this wavenumber limit. This excess component should be negligible in the power spectra of brighter regions. The deviation from the power-law spectrum at scales smaller than $\sim 3'$ can be attributed to the spatial resolution of the *WIDE-L* band, whose point spread function (PSF) is shown as the dotted line in figure 12.

The estimated γ is in good agreement with that estimated by Miville-Deschênes et al. (2010) shown above. The spectra clearly show the wide dynamic range of our observation, as the spatial power component is well retrieved from $> 10°$ large-scale distribution to $< 5'$ small-scale structures.

One advantage of the AKARI FIR data compared to the IRAS data is illustrated in figure 12, which shows deviation from the power-law distribution well above the spatial scales that the AKARI FIR data shows the deviation to be, due to the improved spatial resolution of the AKARI data. The advantage of the improved spatial resolution of the AKARI FIR data is thus clearly indicated.
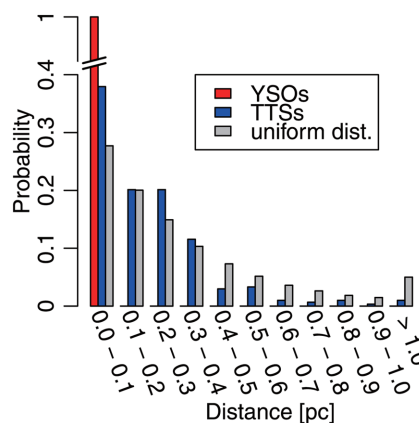
5.2 Filamentary structure

Recent observations by the Herschel satellite show that cirrus clouds consist of filamentary structures, the typical width of which is ~ 0.1 pc (section 1). This typical width corresponds to $3'.4$–$1'.1$ at the distance of 100–300 pc
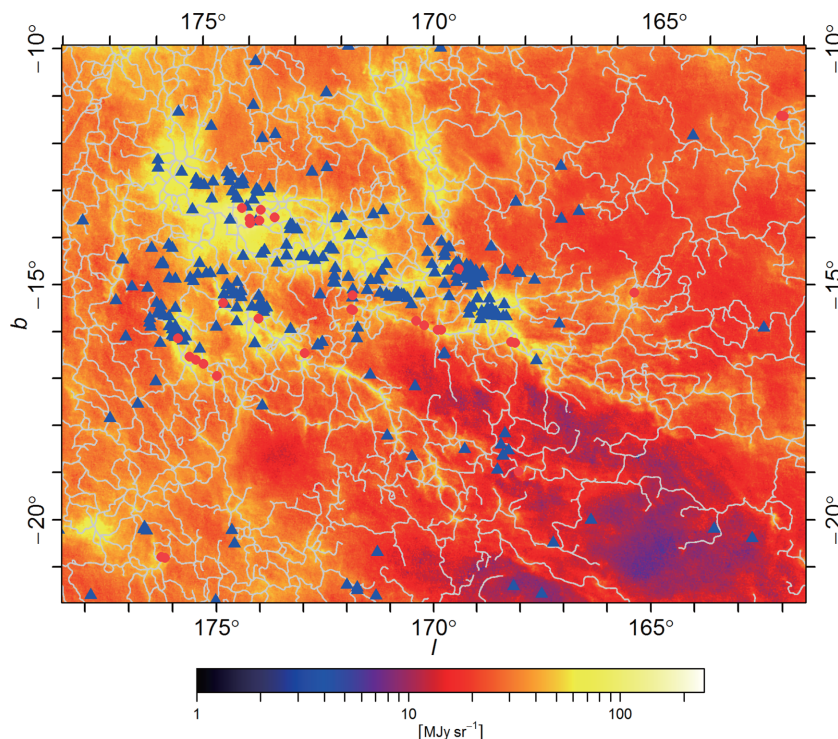
Fig. 13. Filamentary structures extracted from the AKARI all-sky survey image of the Taurus region (Doi et al. 2014). The skeleton of the filamentary structures, which is extracted from the AKARI image by applying the DisPerSE algorithm (Sousbie 2013), is superposed on the AKARI *WIDE-L* all-sky survey image. The red circles are 30 candidate sources of young stellar objects identified in the AKARI bright source catalogue (Tóth et al. 2014). The blue triangles are 303 known T-Tauri stars in the region (Takita et al. 2010), a compilation of published catalogues by Strom et al. (1989), Beckwith et al. (1990), Wichmann et al. (1996), Magazzu et al. (1997), Li and Hu (1998), Güdel et al. (2007), Kenyon, Gómez, and Whitney (2008), and Rebull et al. (2010).

from the Sun. Thus these filaments in the local clouds are detectable in the AKARI images, and the global distribution of the filamentary structures can be revealed by the AKARI all-sky survey (Doi et al. 2014). Figure 13 shows an example of the filamentary structure extraction by applying the DisPerSE algorithm (Sousbie 2013) to an AKARI image of the Taurus molecular cloud (Doi et al. 2014). The ubiquitous distribution of the filamentary structure is displayed.

We also plot candidate sources of young stellar objects (YSOs; Tóth et al. 2014) and known T-Tauri stars (TTSs; Takita et al. 2010) in figure 13 to check their spatial correlation with the filamentary structures (also see figure 14). All the YSO candidates (30 out of 30 sources) in the region show spatial coincidence with the filamentary structure within the range of our spatial resolution. This correspondence is consistent with the Herschel observations (section 1), which found $> 70\%$ of prestellar cores in the filaments (André et al. 2014), indicating a strong connection of the filamentary structures and star-formation activities. TTSs show less concentration at the filaments, but still significantly higher concentration than that expected

Fig. 14. Histogram of the distance from young stellar objects (YSOs; red bars) and T-Tauri stars (TTSs; blue bars) in the region shown in figure 13 to their nearest filamentary structures. Distance to the Taurus region is assumed 137 pc (Torres et al. 2007). All the 30 YSOs show spatial coincidence with the extracted filaments within the range of our spatial resolution (< 0.05 pc). TTSs show moderate concentration at the filaments with the distance < 0.4 pc. The grey bars show an expected distribution of the uniformly distributed sources in the region. The significance of the difference between the distribution of TTSs and that of uniformly distributed sources is estimated p-value $= 0.004$ by the chi-square test.

for uniformly distributed sources in the region with a *p* value of 0.004. Figure 15 shows the correlation between the distance of the TTSs to their nearest neighbour TTSs, which we take as an indicator of the crowdedness of the TTSs' distribution, and the distance of the TTSs to their adjacent filaments. Since we find no correlation in the plot, we conclude that the moderate concentration of the TTSs found in figures 13 and 14 is not because TTSs tend to be
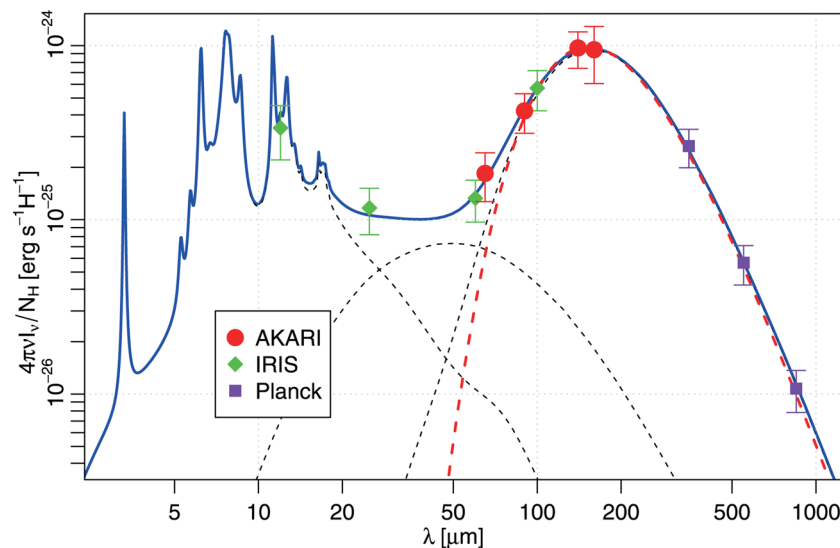
distributed in the dense cirrus regions, which have crowded filamentary structures. This moderate concentration of the TTSs can be explained as an age evolution of their distribution. A proper motion of $0.1\,\mathrm{km\,s^{-1}}$ of the TTSs against their natal filaments for $(1–5) \times 10^6$ yr gives a distance of 0.1–0.5 pc, which is consistent with our observed projected distance of the TTSs from their adjacent filaments.

The large spatial dynamic range of the AKARI observation enables us to reveal global distribution of the filamentary structures, and to study their correlation with young stellar sources of various evolutionary stages.

5.3 Spectral energy distribution

The SED of the cirrus emission can be estimated from the square root of the amplitude of the spatial power spectra (Roy et al. 2010). We estimate the wavelength dependence of the amplitude in the Polaris flare region, the area of which is shown in figure 12. The power-law index of the spectrum scales is assumed as $\gamma = -2.61$ for all four AKARI FIR bands as well as the ancillary data of IRIS and Planck. The estimated relative amplitudes and their fitting errors are shown in figure 16.

In addition to the spatial dynamic range of the AKARI data, another key aspect is its ability to sample across the spectral peak of the dust SED with four photometric wavebands. To demonstrate this aspect, we performed a model

Fig. 15. Correlation between the distance of the TTSs to their nearest neighbour TTSs and the distance of the TTSs to their adjacent filaments. Arrows are the sources who show positional correspondence to filaments within our spatial resolution. The nearest neighbour distance is an indicator of the crowdedness of the TTSs' distribution. We find no dependence of the TTSs' distance to their adjacent filaments whether they are in the crowded regions or in an open field.

Fig. 16. Spectrum energy distribution at the Polaris flare region shown in figure 12 by fitting the spatial power spectra of each observational band by assuming a power-law index of -2.61, which is estimated for the *WIDE-L* data. The square root of the relative amplitude of the spatial power spectra and their fitting errors are shown for the four AKARI FIR data as well as the ancillary IRIS and Planck data. The solid line indicates a model fitting of the four AKARI FIR data by applying the DustEM SED model (Compiègne et al. 2011). The dotted lines are the decomposition of the modelled SED in BGs, SGs (small gains), and PAHs (polycyclic aromatic hydrocarbons). The relative fractions of the excess emission from SGs against that from BGs estimated from the fitted model SED are 70.0% for *N60*, 16.4% for *WIDE-S*, 2.6% for *WIDE-L*, and 2.0% for *N160*. The dashed line indicates the estimation of colour temperature ($T = 16.8$ K) from the intensity ratio between *WIDE-S* and *WIDE-L* data assuming a modified blackbody spectral index $\beta = 1.62$. (Colour online)

fit to the AKARI FIR data with the Compiègne et al. (2011) dust model, using the DustEM numerical tool,[1] as indicated in figure 16. It is clear that we can accurately reproduce the FIR dust SED with the AKARI FIR data, as the fitted model SED agrees well with all the ancillary data.

The colour temperature from the *WIDE-S*/*WIDE-L* intensity ratio (90 μm/140 μm) is estimated to be $T = 16.8$ K. A modified blackbody spectrum of the estimated temperature is shown in figure 16 as the dashed line. A modified blackbody spectral index is assumed $\beta = 1.62$, which is a mean value over the whole sky estimated by Planck Collaboration (2014b) by fitting IRIS 100 μm and Planck 353, 545, and 857 GHz data with modified blackbody spectra. The estimated colour temperature spectrum is consistent with the FIR–sub-mm part of the BGs' emission spectrum as well as the Planck observations.

The AKARI FIR data is therefore a good tracer of the temperature, and of the total amount of BGs, and, as a result, of the ISM as a whole. Together with the much improved spatial resolution from the former all-sky survey data in the FIR wavebands, the newly achieved AKARI FIR high spatial resolution images of the whole sky should be a powerful tool for investigating the detailed spatial structure of ISM and its physical environment.

6 Caveats and plans for future improvements

Although we have produced a sensitive all-sky FIR images, the data still contains some artefacts, and there is scope for further improvements. In the following, we describe remaining caveats about the efficacy of the data and our plans to mitigate these remaining problems.

6.1 Zodiacal emission

Although we have subtracted the smooth cloud component of the ZE from the raw data, we have not yet subtracted the asteroidal dust band component, nor the MMR component from the data, with the consequence that the contributions from these remain in the images and are recognizable at the shorter wavelength bands (*N60* and *WIDE-S*). This is because small-scale structures of the ZE are not adequately reproduced by the former ZE models (subsection 3.2). Asteroidal dust bands appear as pairs of parallel bands equally spaced above and below the ecliptic plane. The continuous and smooth distribution of the dust bands and the MMR component along the ecliptic plane can be seen in the AKARI *N60* and *WIDE-S* maps (figure 9).
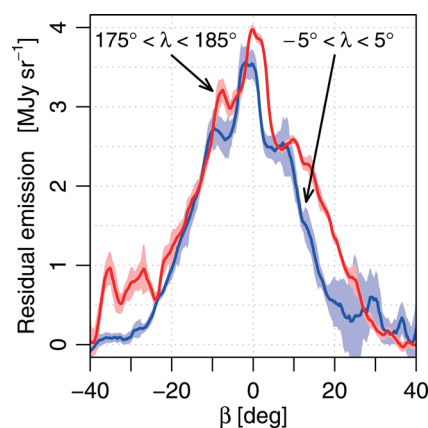
Fig. 17. Example latitudinal profiles of the dust bands and the MMR component observed in the *WIDE-S* band in two regions, $175° < \lambda < 185°$ and $-5° < \lambda < 5°$. The shaded areas denote the standard error of the profile. The intensity of the residual ZE contribution in the AKARI map is less than 5 MJy sr^{-1} at the shorter wavelength bands. (Colour online)

The intensity and the ecliptic latitudes of the peak positions of these components change depending on the ecliptic longitude. We briefly evaluate the spatial distribution and the latitudinal profiles of these components at the shorter wavelength bands, *N60* and *WIDE-S*. The contribution of the asteroidal dust bands and the MMR component will be discussed in more detail in T. Ootsubo et al. (in preparation). Figure 17 shows example latitudinal profiles of the residual ZE contribution from the dust bands and the MMR component observed in the *WIDE-S* band in two regions, where the ZE contributions are strong ($175° < \lambda < 185°$ and $-5° < \lambda < 5°$).

The estimated intensities of the emission that are left in the AKARI FIR images reach maximum near the ecliptic plane and are < 5 MJy sr^{-1} for *N60* and < 4 MJy sr^{-1} for *WIDE-S*. Although the ZE contribution cannot be clearly seen in the *WIDE-L* and *N160* images, the estimated intensities are < 1 MJy sr^{-1} for *WIDE-L* and *N160* at most, if we assume that these components have the dust temperature $T = 200$–300 K.

6.2 Moving bodies

Planets and asteroids have not been masked during our image processing as the detection of the faint sources is not fully investigated and the scattering patterns of the bright sources are yet to be analysed. Thus the images near the ecliptic plane may contain these solar system bodies and will need further consideration in the future. Meanwhile, we list positions of the planets and 55 major asteroids that are scanned during the AKARI FIR all-sky survey observation in table 3.

Table 3. List of planets' and 55 major asteroids' positions that are scanned during the AKARI FIR all-sky survey observation.

Source name	Equatorial coordinates		Galactic coordinates		Ecliptic coordinates	
	RA (J2000.0) (h m s)	Dec (J2000.0) (° ′ ″)	l (° ′ ″)	b (° ′ ″)	λ (° ′ ″)	β (° ′ ″)
Philomela	0 23 20	13 10 12	113 27 40	−48 57 18	10 36 32	9 46 07
Interamnia	0 45 40	9 05 33	121 37 09	−53 29 55	14 02 59	3 51 15
Emma	1 46 58	11 12 19	144 56 03	−48 54 60	28 50 02	0 09 15
Juno	1 52 50	5 19 21	150 37 56	−53 49 35	28 06 34	−5 51 41
Aurora	2 02 41	−5 16 59	164 42 45	−61 46 38	26 37 40	−16 39 05
Isis	2 11 22	8 30 20	154 58 10	−48 55 39	33 32 49	−4 27 20
Wratislavia	2 15 31	13 19 50	153 00 36	−44 11 01	36 06 47	−0 14 36
Fides	2 18 36	20 27 01	149 44 12	−37 27 58	39 09 44	6 14 08
Bellona	2 36 59	9 14 59	162 17 52	−44 58 36	39 47 58	−5 47 36
Thisbe	2 49 41	13 44 55	162 15 11	−39 30 26	44 08 06	−2 26 35
Juno	3 03 34	28 51 30	155 25 07	−25 09 50	51 35 47	11 06 23
Pallas	3 05 26	10 11 17	169 02 57	−39 56 55	46 49 11	−6 57 14
Athamantis	3 10 38	11 46 18	168 58 07	−37 55 01	48 29 17	−5 46 41
Uranus	3 14 48	23 18 07	161 17 27	−28 16 60	52 30 58	5 04 25
Uranus	3 18 39	9 04 28	173 08 19	−38 35 26	49 41 16	−8 54 08
Herculina	3 23 38	22 21 32	163 46 00	−27 46 52	54 14 39	3 38 18
Palma	3 35 10	32 19 34	159 11 41	−18 23 14	59 13 37	12 40 18
Melpomene	3 36 35	5 07 32	180 41 56	−38 06 12	53 04 22	−13 50 19
Emma	4 06 26	19 17 60	174 10 29	−23 10 55	63 19 29	−1 33 04
Philomela	5 17 30	6 36 23	195 59 57	−16 50 58	78 59 35	−16 25 49
Euphrosyne	6 00 57	7 30 24	200 43 43	−7 04 04	90 14 49	−15 56 06
Hesperia	6 32 01	28 10 53	185 55 37	9 10 22	97 04 39	4 56 09
Thetis	7 14 39	22 26 34	195 23 44	15 30 15	107 12 06	0 06 30
Themis	7 50 56	10 22 05	210 38 56	18 25 14	117 44 32	−10 26 33
Minerva	7 51 35	24 25 59	196 49 42	24 06 00	115 15 31	3 24 16
Lutetia	8 05 09	22 44 33	199 46 51	26 25 16	118 38 33	2 21 29
Diotima	8 11 14	18 49 09	204 26 18	26 19 50	120 51 43	−1 10 35
Io	8 13 18	16 02 16	207 30 29	25 43 15	121 57 01	−3 47 02
Callisto	8 18 17	20 57 56	202 51 45	28 39 19	122 00 21	1 16 59
Lutetia	8 21 13	9 51 47	214 36 36	24 55 15	125 14 41	−9 21 50
Astraea	8 28 39	19 49 45	205 04 20	30 31 25	124 37 52	0 44 37
Nemausa	8 30 12	18 11 16	207 00 02	30 16 21	125 23 06	−0 45 37
Thetis	8 46 27	39 54 50	182 19 16	38 59 22	123 05 57	21 08 01
Emma	8 48 57	45 19 03	175 22 18	39 44 09	121 51 50	26 26 16
Herculina	8 55 19	21 25 53	205 48 29	36 56 08	130 14 57	3 54 13
Loreley	8 55 39	15 40 07	212 29 54	34 57 38	131 55 05	−1 36 48
Pallas	9 01 57	16 18 36	212 28 57	36 36 07	133 11 22	−0 34 29
Jupiter	9 01 60	43 41 13	177 32 14	42 03 25	124 52 60	25 35 57
Minerva	9 03 39	12 07 55	217 24 52	35 18 02	134 46 50	−4 27 39
Pluto	9 14 34	31 28 08	194 26 06	43 35 25	131 27 15	14 45 29
Metis	9 17 31	19 21 60	210 32 14	41 09 39	135 50 15	3 26 01
Amphitrite	9 24 59	16 32 36	214 54 22	41 48 08	138 23 38	1 17 23
Diotima	9 29 38	4 47 15	229 13 33	37 30 50	143 11 19	−9 30 46
Hygiea	9 31 55	18 38 34	213 03 26	44 06 27	139 18 21	3 48 11
Doris	9 32 60	9 28 22	224 30 58	40 33 33	142 28 33	−4 48 25
Metis	9 34 18	23 32 55	206 41 22	46 09 38	138 15 01	8 37 39
Victoria	9 37 38	13 37 39	220 11 55	43 26 03	142 12 52	−0 30 27
Doris	9 43 41	17 06 07	216 31 47	46 09 36	142 27 34	3 15 11
Europa	9 45 03	12 33 42	222 37 22	44 36 15	144 16 20	−0 55 23
Harmonia	9 49 12	14 17 53	221 00 34	46 15 40	144 38 35	1 02 58
Germania	9 55 59	3 33 08	235 13 51	42 22 05	149 52 47	−8 29 32

Table 3. (Continued)

Source name	Equatorial coordinates		Galactic coordinates		Ecliptic coordinates	
	RA (J2000.0)	Dec (J2000.0)	*l*	*b*	λ	β
	(ʰ m s)	(° ′ ″)	(° ′ ″)	(° ′ ″)	(° ′ ″)	(° ′ ″)
Wratislavia	10 10 52	19 11 33	217 07 28	52 56 14	147 49 51	7 26 05
Patientia	10 27 59	14 33 07	227 07 58	54 49 17	153 21 24	4 35 27
Ino	10 34 06	4 57 30	241 50 18	50 50 31	158 17 42	−3 46 23
Germania	10 37 02	3 02 46	244 53 16	50 10 52	159 41 35	−5 16 27
Ceres	11 01 14	12 10 36	238 45 52	60 32 34	161 46 26	5 26 43
Iris	11 09 10	−1 14 44	258 58 11	52 37 38	168 47 48	−6 10 06
Amphitrite	11 12 56	17 02 15	233 01 02	65 31 55	162 28 51	11 01 30
Patientia	11 18 07	9 34 37	248 25 02	62 08 09	166 37 15	4 39 55
Neptune	11 28 04	−7 48 37	271 00 13	49 42 29	175 47 29	−10 20 10
Hebe	11 46 52	−0 59 25	272 43 25	57 55 10	177 22 49	−2 12 53
Davida	11 55 49	11 54 11	261 34 52	70 06 40	174 15 10	10 29 35
Cybele	12 00 21	12 22 41	263 26 31	71 08 58	175 05 28	11 22 38
Neptune	12 00 43	2 37 33	275 56 20	62 40 04	179 07 12	2 28 50
Cybele	12 03 06	−13 02 02	286 08 37	48 03 43	185 58 03	−11 38 03
Neptune	12 11 14	−3 14 42	284 58 44	58 01 51	183 51 56	−1 51 41
Wratislavia	12 14 11	−2 55 29	286 10 10	58 32 08	184 24 56	−1 16 28
Fortuna	12 20 58	−1 22 22	288 41 02	60 26 51	185 21 23	0 49 22
Ceres	12 21 50	5 23 20	285 25 25	67 03 35	182 51 45	7 06 52
Aglaja	12 27 03	2 27 40	290 10 28	64 30 53	185 14 00	4 56 44
Daphne	12 32 16	6 57 25	291 15 10	69 10 32	184 37 58	9 35 15
Thalia	12 44 00	−3 45 59	300 35 32	58 48 37	191 35 11	0 53 13
Ceres	13 08 18	2 54 00	314 29 59	65 04 09	194 36 54	9 23 11
Chicago	13 10 03	−16 27 29	310 15 06	45 50 46	202 25 33	−8 20 43
Interamnia	13 18 53	−3 03 17	317 28 22	58 42 19	199 21 43	4 53 04
Cava	13 22 06	−10 32 57	316 03 07	51 12 44	202 54 26	−1 46 05
Athamantis	13 27 34	1 27 04	324 13 40	62 27 17	199 41 17	9 52 34
Ino	13 28 52	−3 08 24	322 01 39	57 58 59	201 43 08	5 44 11
Daphne	13 30 38	−11 34 48	318 53 31	49 44 04	205 14 09	−1 57 01
Aglaja	13 39 28	−6 15 17	324 47 24	54 12 06	205 19 39	3 48 12
Melete	13 45 06	−19 16 05	320 45 11	41 23 42	211 17 57	−7 50 48
Isis	14 12 49	7 45 23	352 11 01	62 05 02	208 10 36	19 51 25
Melete	14 26 45	−11 17 07	337 45 35	44 38 07	218 02 42	3 04 09
Fides	14 31 33	−13 50 35	337 19 37	41 50 21	219 58 05	1 00 51
Melpomene	14 40 19	−7 48 59	344 26 12	45 39 49	220 08 38	7 24 39
Bellona	15 08 34	−12 02 30	348 15 37	38 02 16	228 04 29	5 22 55
Uranus	15 12 44	−5 09 16	355 21 15	42 25 22	227 11 14	12 17 26
Palma	15 17 14	−17 59 26	345 35 23	32 07 22	231 40 26	0 12 05
Saturn	15 31 58	−15 34 25	350 35 36	31 37 41	234 29 23	3 25 22
Massalia	15 39 08	−17 48 43	350 16 28	28 49 20	236 41 01	1 38 58
Euphrosyne	16 05 18	−11 59 28	0 01 59	28 14 54	241 39 08	8 40 22
Eleonora	16 17 46	−13 55 52	0 33 04	24 40 25	245 01 39	7 19 20
Dione	16 27 22	−19 44 08	357 19 29	19 11 41	248 15 38	1 58 32
Jupiter	16 49 42	−19 10 27	1 12 54	15 25 14	253 24 08	3 15 39
Europa	17 04 44	−16 10 36	5 53 47	14 16 03	256 39 03	6 37 38
Chaldaea	17 09 43	−22 13 01	1 31 08	9 50 44	258 22 35	0 43 09
Chaldaea	17 10 22	−22 13 47	1 35 42	9 42 60	258 31 32	0 43 09
Carlova	17 11 30	−31 19 26	354 16 49	4 13 49	259 33 05	−8 19 15
Flora	17 18 19	−18 10 20	6 04 02	10 27 46	260 04 05	4 54 40
Thisbe	17 34 27	−22 35 50	4 24 04	4 53 02	264 06 09	0 42 50
Massalia	17 35 19	−16 02 40	10 06 06	8 11 16	264 01 21	7 16 10
Carlova	18 08 16	−21 32 39	9 18 29	−1 18 59	271 55 18	1 53 02
Papagena	18 13 16	9 03 60	37 03 53	12 02 43	273 52 51	32 27 50

Table 3. (Continued)

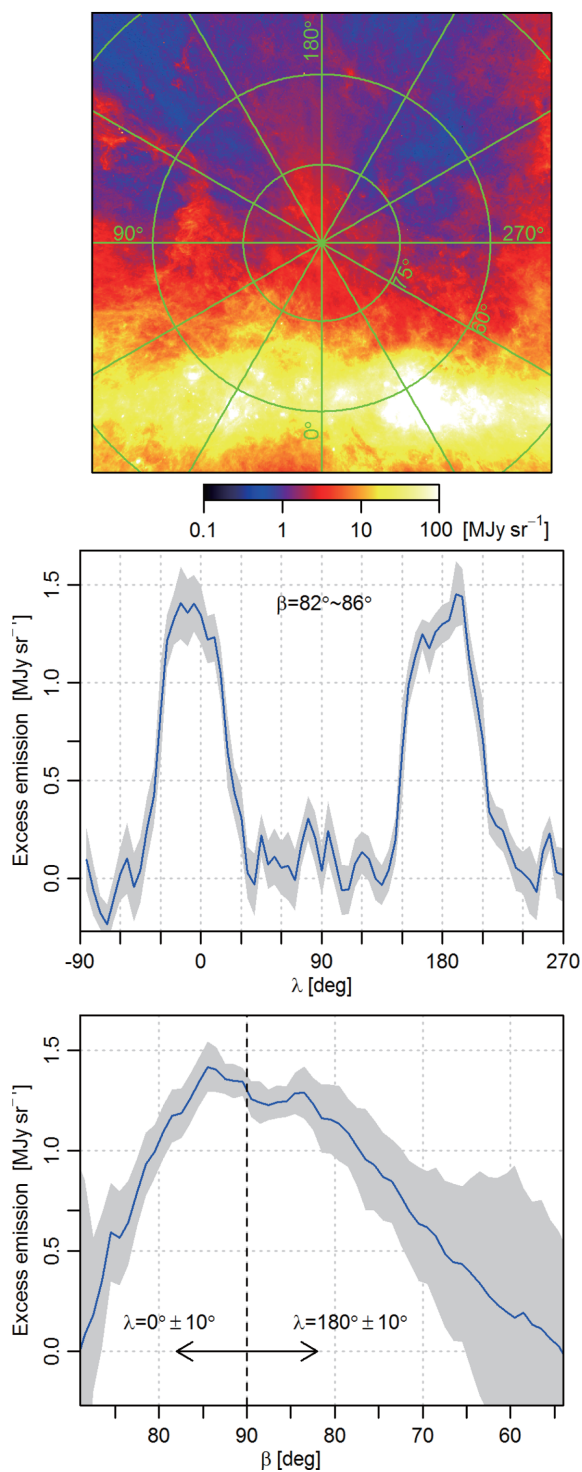| Source name	Equatorial coordinates		Galactic coordinates		Ecliptic coordinates	
	RA (J2000.0) (^{h} ^{m} ^{s})	Dec (J2000.0) ($^\circ$ $'$ $''$)	l ($^\circ$ $'$ $''$)	b ($^\circ$ $'$ $''$)	λ ($^\circ$ $'$ $''$)	β ($^\circ$ $'$ $''$)
Berbericia	18 18 32	−23 43 42	8 31 17	−4 26 29	274 14 23	−0 21 17
Saturn	19 21 02	−26 55 24	11 39 58	−18 34 54	288 02 46	−4 44 31
Nemausa	19 22 52	−20 18 05	18 14 10	−16 23 49	289 23 14	1 45 25
Victoria	19 34 33	−22 34 06	17 09 42	−19 47 10	291 44 06	−0 53 33
Hygiea	19 39 12	−28 07 41	12 00 14	−22 46 21	291 51 33	−6 32 55
Vesta	19 44 49	−17 09 29	23 27 30	−19 53 53	295 01 25	4 02 09
Saturn	20 25 57	−14 11 06	30 46 19	−27 47 01	305 21 16	4 53 27
Aurora	20 30 03	−7 57 06	37 34 38	−26 02 09	307 51 45	10 41 45
Papagena	20 30 43	−28 19 40	15 43 03	−33 38 16	303 01 05	−9 06 09
Davida	20 37 04	−16 50 20	29 10 08	−31 17 10	307 18 16	1 39 46
Astraea	20 39 53	−8 44 37	38 00 16	−28 33 47	310 02 47	9 18 56
Cava	20 42 24	−18 50 03	27 31 44	−33 12 05	308 01 21	−0 35 26
Chicago	20 50 21	−8 57 51	39 06 38	−30 58 29	312 30 38	8 24 57
Themis	21 03 18	−19 31 48	28 51 08	−38 03 57	312 34 52	−2 36 14
Io	21 17 58	−15 57 27	34 46 19	−40 01 20	316 58 14	−0 12 59
Dione	21 18 06	−23 41 38	25 04 01	−42 38 05	314 38 54	−7 35 54
Iris	21 28 39	−15 05 14	37 10 17	−42 03 07	319 41 22	−0 10 59
Loreley	21 29 52	−26 16 36	22 31 29	−45 52 12	316 23 40	−10 53 11
Amphitrite	21 37 23	−14 26 59	39 07 56	−43 43 18	321 53 28	−0 15 02
Hygiea	21 41 05	−20 01 50	32 14 23	−46 36 38	320 54 25	−5 48 54
Fortuna	21 47 12	5 46 46	63 04 34	−34 58 56	331 05 24	18 00 21
Alexandra	21 52 02	−21 03 50	31 59 37	−49 22 08	322 59 27	−7 38 47
Flora	22 03 01	−1 42 44	58 38 59	−42 43 16	332 11 43	9 36 19
Davida	22 17 30	−0 01 40	63 34 53	−44 30 29	336 14 09	9 52 54
Eleonora	22 30 08	−10 17 20	53 51 56	−53 09 01	335 24 43	−0 49 05
Germania	22 45 13	−14 13 16	51 15 39	−58 20 10	337 22 00	−5 50 27
Hebe	22 47 60	10 22 26	81 01 41	−42 11 03	347 30 31	16 37 37
Thalia	22 50 15	−8 14 16	61 42 34	−56 01 22	340 47 03	−0 46 19
Alexandra	23 04 20	−6 47 27	67 52 12	−57 44 27	344 33 42	−0 46 18
Harmonia	23 18 57	−5 15 21	74 53 45	−59 11 27	348 30 36	−0 46 20
Hesperia	23 50 09	−14 35 13	73 07 30	−71 14 56	351 51 23	−12 23 13

6.3 Earth shine

During the survey observation, the pointing direction of the telescope was kept orthogonal to the Sun–Earth direction and away from the centre of the Earth, so that we can minimize the heat input from the Earth to the telescope (section 2). However, since the inclination angle of the satellite's orbit was not equal to 90°, the satellite direction was not precisely in the opposite direction to the centre of the Earth and had a small time variation. This resulted in a small variation in the viewing angle of the Earth limb from the telescope. The viewing angle reached its minimum in the observation around the north ecliptic pole during the summer solstice period and caused the illumination of the Earth's thermal radiation to the top end of the telescope structure above the baffle around the telescope. This thermal radiation was detected as the excess emission in the all-sky survey image, and is most conspicuous in the *WIDE-S* band images with a maximum intensity of

~ 1.5 MJy sr^{-1}. The contaminated regions are spread like a fan around the north ecliptic pole at around λ: −30°– +20°, $\beta \geq 71$° and λ: +150°– +210°, $\beta \geq 54$°. The cross section of the spatial profile of the excess emission is shown in figure 18. Since the spatial profile is not well determined because the scattering path of the Earth shine in the telescope is not fully studied yet, we leave the emission in the production image and alert the attention of the users of the image data. Assuming a 300 K blackbody spectrum for the Earth shine, the excess emission of 1.5 MJy sr^{-1} in the *WIDE-S* band corresponds to 2.2, 0.13, and 0.05 MJy sr^{-1} in *N60*, *WIDE-L*, and *N160* bands, respectively.

7 Data release

We made the first data release of our all-sky survey data to the public in 2014 December. The data are released as $6° \times 6°$ FITS format intensity image tiles that cover the

whole sky, with supporting data showing the standard deviation of intensity, data sample numbers, and number of spatial scans in the same two-dimensional FITS files.[2]

8 Conclusion

We provide full-sky images of the AKARI FIR survey at 65 µm, 90 µm, 140 µm, and 160 µm. Together with the > 99% coverage of the whole sky, the high spatial resolution from 1′ to 1′.5 of the AKARI FIR survey reveals the large-scale distribution of ISM with great detail. Comprehensive wavelength coverage from 50 to 180 µm with four photometric bands provides SED information at the peak of the dust continuum emission, enabling us to make precise evaluation of its temperature, which leads to a detailed investigation of the total amount of dust particles and its irradiation environment. The AKARI FIR images are a new powerful resource from which we investigate the detailed nature of ISM from small scales to the full sky.

References

Arzoumanian, D., et al. 2011, A&A, 529, L6
Arzoumanian, D., André, P., Peretto, N., & Könyves, V. 2013, A&A, 553, A119
André, P. 2015, in Highlights of Astronomy, Vol. 16, ed. T. Montmerle (Cambridge: Cambridge University Press), 31
André, P., et al. 2010, A&A, 518, L102
André, P., di Francesco, J., Ward-Thompson, D., Inutsuka, S., Pudritz, R. E., & Pineda, J. 2014, in Protostars and Planets VI, ed. H. Beuther et al. (Tucson: University of Arizona Press), 27
Beckwith, S. V. W., Sargent, A. I., Chini, R. S., & Guesten, R. 1990, AJ, 99, 924
Beichman, C. A., Neugebauer, G., Habing, H. J., Clegg, P. E., & Chester, T. J. 1988, Infrared Astronomical Satellite (IRAS) Catalogs and Atlases. Volume 1: Explanatory Supplement (Washington, D.C.: NASA)

---

[2] All the data can be retrieved from the following web site: ⟨http://www.ir.isas.jaxa.jp/ASTRO-F/Observation/⟩.

Fig. 18. Top panel: *WIDE-S* image of the north ecliptic pole. A fan-like distribution of the excess emission due to Earth shine is recognizable. Middle and bottom panels: cross sections of the excess emission in the *WIDE-S* image. The shaded areas denote the standard deviation of the profile. (Colour online)

Bernard, J. P., et al. 1999, A&A, 347, 640

Bernard, J.-P., et al. 2010, A&A, 518, L88

Berriman, G. B., Good, J. C., Laity, A. C., & Kong, M. 2008, in ASP Conf. Ser., 394, Astronomical Data Analysis Software and Systems XVII, ed. R. W. Argyle et al. (San Francisco: ASP), 83

Boggess, N. W., et al. 1992, ApJ, 397, 420

Boulanger, F., Abergel, A., Bernard, J.-P., Burton, W. B., Desert, F.-X., Hartmann, D., Lagache, G., & Puget, J.-L. 1996, A&A, 312, 256

Boulanger, F., & Perault, M. 1988, ApJ, 330, 964

Compiègne, M., et al. 2011, A&A, 525, A103

Compiègne, M., Flagey, N., Noriega-Crespo, A., Martin, P. G., Bernard, J.-P., Paladini, R., & Molinari, S. 2010, ApJ, 724, L44

Désert, F.-X., Boulanger, F., & Puget, J. L. 1990, A&A, 237, 215

Doi, Y., et al. 2009, ASP Conf. Ser., 418, 387

Doi, Y., et al. 2012, Publ. Korean Astron. Soc., 27, 111

Doi, Y., et al. 2014, Publi. Korean Astron. Soc., submitted

Draine, B. T. 2003, ARA&A, 41, 241

Draine, B. T., &, Li A. 2007, ApJ, 657, 810

Gautier, T. N., Boulanger, F., III, Perault, M., & Puget, J. L. 1992, AJ, 103, 1313

Gorjian, V., Wright, E. L., & Chary, R. R. 2000, ApJ, 536, 550

Güdel, M., et al. 2007, A&A, 468, 353

Hauser, M.G., Kelsall, T., Leisawitz, D., & Weiland, J. ed. 1988, COBE Diffuse Infrared Background Experiment (DIRBE) Explanatory Supplement COBE Ref. Pub. No. 97-A (Greenbelt, MD: NASA/GSFC)

Jeong, W.-S., Mok Lee, H., Pak, S., Nakagawa, T., Minn Kwon, S., Pearson, C. P., & White, G. J. 2005, MNRAS, 357, 535

Joncas, G., Boulanger, F., & Dewdney, P. E. 1992, ApJ, 397, 165

Kaneda, H., et al. 2009, PASP, 121, 549

Kawada, M., et al. 2007, PASJ, 59, S389

Kelsall, T., et al. 1998, ApJ, 508, 44

Kennicutt, R. C., Jr. 1998, ARA&A, 36, 189

Kenyon, S. J., Gómez, M., & Whitney, B. A. 2008, Handbook of Star Forming Regions, Volume I (San Francisco: ASP)

Kiss, C., Ábrahám, P., Klaas, U., Juvela, M., & Lemke, D. 2001, A&A, 379, 1161

Kiss, C., Ábrahám, P., Klaas, U., Lemke, D., Héraudeau, P., del Burgo, C., & Herbstmeier, U. 2003, A&A, 399, 177

Könyves, V., et al. 2010, A&A, 518, L106

Lagache, G., Abergel, A., Boulanger, F., & Puget, J.-L. 1998, A&A, 333, 709

Lagache, G., Haffner, L. M., Reynolds, R. J., & Tufte, S. L. 2000, A&A, 354, 247

Li, J. Z., & Hu, J. Y. 1998, A&AS, 132, 173

Low, F. J., et al. 1984, ApJ, 278, L19

Magazzu, A., Martin, E. L., Sterzik, M. F., Neuhauser, R., Covino, E., & Alcala, J. M. 1997, A&AS, 124, 449

Martin, P. G., et al. 2010, A&A, 518, L105

Mathis, J. S. 1990, ARA&A, 28, 37

Mathis, J. S., Mezger, P. G., & Panagia, N. 1983, A&A, 128, 212

Meisner, A. M., & Finkbeiner, D. P. 2015, ApJ, 798, 88

Miville-Deschênes, M.-A., et al. 2010, A&A, 518, L104

Miville-Deschênes, M.-A., & Lagache, G. 2005, ApJS, 157, 302

Miville-Deschênes, M.-A., Lagache, G., Boulanger, F., & Puget, J.-L. 2007, A&A, 469, 595

Miville-Deschênes, M.-A., Lagache, G., & Puget, J.-L. 2002, A&A, 393, 749

Murakami, H., et al. 2007, PASJ, 59, S369

Nagata, H., Shibai, H., Hirao, T., Watabe, T., Noda, M., Hibi, Y., Kawada, M., & Nakagawa, T. 2004, IEEE Trans. Electron Devices, 51, 270

Nakagawa, T., et al. 2007, PASJ, 59, S377

Neugebauer, G., et al. 1984, ApJ, 278, L1

Onaka, T., et al. 2007, PASJ, 59, S401

Pilbratt, G. L., et al. 2010, A&A, 518, L1

Planck Commentoration 2011, A&A, 536, A19

Planck Collaboration 2014a, A&A, 571, A1

Planck Collaboration 2014b, A&A, 571, A11

Planck Collaboration 2014c, arXiv:1409.2495

Poglitsch, A., et al. 2010, A&A, 518, L2

Pyo, J., et al. 2010, A&A, 523, A53

Rebull, L. M., et al. 2010, ApJS, 186, 259

Roy, A., et al. 2010, ApJ, 708, 1611

Shirahata, M., et al. 2009, PASJ, 61, 737

Schlegel, D. J., Finkbeiner, D. P., & Davis, M. 1998, ApJ, 500, 525

Sousbie, T. 2013, Astrophysics Source Code Library, 1302.015 〈http://ascl.net/1302.015〉

Strom, K. M., Strom, S. E., Edwards, S., Cabrit, S., & Skrutskie, M. F. 1989, AJ, 97, 1451

Suzuki, T., et al. 2008, PASP, 120, 895

Takita, S., et al. 2015, PASJ, 67, 49

Takita, S., Kataza, H., Kitamura, Y., Ishihara, D., Ita, Y., Oyabu, S., & Ueno, M. 2010, A&A, 519, A83

Torres, R. M., Loinard, L., Mioduszewski, A. J., & Rodríguez, L. F. 2007, ApJ, 671, 1813

Tóth, L. V., et al. 2014, PASJ, 66, 17

Ward-Thompson, D., et al. 2010, A&A, 518, L92

Wheelock, S. L., et al. 1994, IRAS Sky Survey Atlas: Explanatory Supplement, NASA STI/Recon Technical Report No. 95-22539 (Washington D.C.: NASA)

Wichmann, R., et al. 1996, A&A, 312, 439

Wright, E. L. 1998, ApJ, 496, 1

Yamamura, I., et al. 2009, in ASP Conf. Ser. 418, AKARI, a Light to Illuminate the Misty Universe, ed. T. Onaka et al. (San Francisco: ASP), 3